DO BARS DRIVE SPIRAL DENSITY WAVES?

Ronald J. Buta[1], Johan H. Knapen[2], Bruce G. Elmegreen[3], Heikki Salo[4], Eija Laurikainen[4], Debra
Meloy Elmegreen[5], Ivânio Puerari[6], and David L. Block[7]
[1] Department of Physics and Astronomy, University of Alabama, Tuscaloosa, AL 35487, USA; rbuta@bama.ua.edu
[2] Instituto de Astrofísica de Canarias, E-38200 La Laguna, Spain; jhk@iac.es
[3] IBM Research Division, T.J. Watson Research Center, 1101 Kitchawan Road, Yorktown Heights, NY 10598, USA; bge@watson.ibm.com
[4] Division of Astronomy, Department of Physical Sciences, University of Oulu, Oulu FIN-90014, Finland; hsalo@sun3.oulu.fi, eija@sun3.oulu.fi
[5] Vassar College, Department of Physics & Astronomy, Box 745, Poughkeepsie, NY 12604, USA; elmegreen@vassar.edu
[6] Instituto Nacional de Astrofísica, Optica y Electrónica, Tonantzintla, PUE 72840, Mexico; puerari@inaoep.mx
[7] Anglo American Cosmic Dust Laboratory, School of Computational & Applied Mathematics, University of the Witwatersrand, P.O. Box 60 Wits, 2050, South
Africa; David.Block@wits.ac.za
Received 2008 October 22; accepted 2009 February 28; published 2009 April 7

ABSTRACT

We present deep near-infrared K_s-band Anglo-Australian Telescope Infrared Imager and Spectrograph observations
of a selected sample of nearby barred spiral galaxies, including some with the strongest known bars. The
sample covers a range of Hubble types from SB0$^-$ to SBc. The goal is to determine if the torque strengths of
the spirals correlate with those of the bars, which might be expected if the bars actually drive the spirals as
has been predicted by theoretical studies. This issue has implications for interpreting bar and spiral fractions
at high redshift. Analysis of previous samples suggested that such a correlation exists in the near-infrared,
where effects of extinction and star formation are less important. However, the earlier samples had only a
few excessively strong bars. Our new sample largely confirms our previous studies, but still any correlation
is relatively weak. We find two galaxies, NGC 7513 and UGC 10862, where there is only a weak spiral in
the presence of a very strong bar. We suggest that some spirals probably are driven by their bars at the same
pattern speed, but that this may be only when the bar is growing or if there is abundant gas and dissipation.

Key words: galaxies: kinematics and dynamics – galaxies: photometry – galaxies: spiral – galaxies: structure

1. INTRODUCTION

The bar phenomenon is a pervasive and complex aspect of
disk galaxies. A bar can be identified in ∼60% or more of
present-epoch disk galaxies (Knapen et al. 2000; Laurikainen
et al. 2004; Menendez-Delmestre et al. 2007; Marinova & Jo-
gee 2007). Studies of galaxies in the GEMS and GOODS fields
suggest that this fraction has been largely constant to at least
$z = 1$ (Elmegreen et al. 2004; Jogee et al. 2004). Results from
a larger sample in the COSMOS field indicates that the bar
fraction is approximately constant out to $z = 0.84$ for the most
massive galaxies only, and that smaller and less massive galax-
ies have a significantly declining bar fraction out to that redshift
(Sheth et al. 2008). There is also a slight correlation between
the presence of a bar and the presence of a prominent bulge
among the high redshift galaxies; this is consistent with the
massive galaxies having a constant bar fraction, since those
galaxies tend to have a bulge (Sheth et al. 2008). Another is-
sue is the effect of environment on bar fraction. Verley et al.
(2007) showed that in a sample of isolated galaxies, a com-
parable fraction is barred as in samples not selected for isola-
tion. Isolated barred galaxies were also found to have a com-
parable distribution of bar strengths to a nonisolation-selected
sample.

An important question is how the strength of a bar impacts the
features seen in a barred galaxy. We are particularly interested
in the relation between the strength of a bar and the appearance
or strength of a spiral. Is there a correlation between bar
strength and spiral arm strength, as suggested by theoretical
models? For example, Yuan & Kuo (1997; see also Kormendy
& Norman 1979; Elmegreen & Elmegreen 1985) showed that
stronger bars excited sharper gaseous density waves than weaker
bars, although other parameters also affected the appearance

of the waves. The fact that some strong observed bars join to
a strong two-armed global spiral suggests that the bars and
spirals are closely connected and that a bar strength–spiral
strength correlation may be present. These global spirals are
so tightly connected to the bar that it would seem the two
features have the same pattern speed. Two-armed spirals around
strong bars are rather common, representing ≈70% of typical
field spirals, unlike nonbarred field spirals where only ≈30%
are two-armed (Elmegreen & Elmegreen 1982). We consider
this bar–spiral correlation as evidence for interaction between
the bar and the spiral, but do not know the nature of the
interaction. It could be through various resonances, for example,
and the exact resonances would determine the ratio of pattern
speeds.

On the other hand, many bars are not connected to global
two-armed spirals. There are bars with flocculent blue arms
around them, galaxies with tiny bars and long irregular (swing
amplified?) types of spirals around them, multiple-armed pat-
terns, and old bars (SB0) with no spiral around them. It is clear
that there is a wide variety in bar–disk interactions that do not
include driving. There are no complete theoretical models that
examine bar-driven density waves that consider both gas and
stars.

We suspect that bars may drive spirals only when (a) the bar
is young and growing in strength itself, or (b) there is ample
gas in the bar–spiral system. Each of these situations provides
an "arrow of time" for the spiral to know whether to be leading
or trailing (Lynden-Bell & Ostriker 1967). Dissipation, growth,
and interactions provide this but a steady state does not (e.g.,
Toomre 1969, 1981). Elmegreen & Elmegreen (1985) suggested
that strong bars can grow to extend all the way to corotation and
organize the gas clouds along strong outer spiral shocks.
The issue of whether bars drive spirals is fundamental to our

Table 1
Revised Classifications and Orientation Parameters

Galaxy	Type	$\langle q \rangle$ Disk	$\langle \phi \rangle$ Disk	$\langle \phi \rangle$ Bar	Range (″)	FWHM (pixel)	Ori. (parsec)
1	2	3	4	5	6	7	8
NGC 175	SB(rs)ab	0.965 ± 0.002	32.5 ± 1.5	125.1	54–74	3.06	K_s
NGC 521	SB(rs)bc	0.980 ± 0.002	25.8 ± 7.3	157.3	94–111	2.47	B
NGC 613	SB(rs)bc	0.749 ± 0.003	121.5 ± 0.4	122.8	150–205	2.59	B
NGC 986	(R'_1)SB(rs)b	0.822 ± 0.001	141.6 ± 2.0	54.8	111–123	2.98	R
NGC 1300	SB(s)b	0.849 ± 0.019	117.2 ± 1.2	106.6	185–195	2.85	B
NGC 1566	(R'_1)SAB(s)bc	0.887 ± 0.004	49.2 ± 0.8	17.2, 2.7	117–153	3.29	B
NGC 4593	(R')SB(rs)ab	0.737 ± 0.004	99.5 ± 0.5	54.2	117–127	3.21	B
NGC 5101	$(R_1R'_2)$SB(rs)a	0.929 ± 0.003	145.0 ± 0.5	121.4	164–184	2.95	B
NGC 5335	SB(r)b	0.844 ± 0.003	95.4 ± 0.6	152.7	51–67	3.76	K_s
NGC 5365	(R)SB0$^-$	0.583 ± 0.002	6.8 ± 0.4	112.0	85–105	2.60	K_s
NGC 6221	SB(s)bc pec	0.665 ± 0.009	12.4 ± 0.3	113.9	110–164	2.64	B
NGC 6384	SAB(r)bc	0.605 ± 0.003	30.6 ± 0.3	35.9	230–261	2.72	B
NGC 6782	$(R_1R'_2)$SB(r)a	0.894 ± 0.002	34.3 ± 0.5	177.9	70–89	2.63	B
NGC 6907	SAB(s)bc	0.837 ± 0.003	69.5 ± 0.6	93.8	87–106	4.10	B
NGC 7155	SB(r)0°	0.950 ± 0.006	49.9 ± 5.3	95.9	77–88	2.78	K_s
NGC 7329	SB(r)b	0.775 ± 0.001	119.0 ± 0.1	76.0	132–140	2.51	B
NGC 7513	SB(s)b	0.675 ± 0.020	104.6 ± 0.3	70.8	74–104	2.80	K_s
NGC 7552	(R'_1)SB(s)ab	0.910 ± 0.008	184.7 ± 3.5	92.9	102–124	4.31	B
NGC 7582	(R'_1)SB(s)ab	0.446 ± 0.002	150.4 ± 0.1	156.1	189–219	3.18	B
IC 1438	$(R_1R'_2)$SAB(r)a	0.862 ± 0.002	128.6 ± 0.9	123.0	90–100	4.83	opt
IC 4290 [a]	(R')SB(r)a	0.906	48.4	97.6		2.45	opt, kin
IC 5092	(R)SB(s)c	0.906 ± 0.004	32.3 ± 0.7	106.3	73–88	2.62	K_s
UGC 10862	SB(rs)c	0.920 ± 0.003	164.9 ± 2.0	35.8	82–92	3.28	K_s

Notes. Column 1: galaxy name; Column 2: classification either from the de Vaucouleurs Atlas of Galaxies (Buta et al. 2007) or in the same system by R. Buta; Column 3: mean disk axis ratio and mean error of ellipse fits to isophotes, based on B or near-IR images as indicated in Column 8; Column 4: mean disk position angle (degrees) based on same ellipse fits, in frame of the K_s-band image. J2000 position angles may be derived as ϕ(disk, J2000) $= \langle \phi \rangle$(disk)+0°.58; Column 5: bar position angle (degrees) based on ellipse fits to bar isophotes on K_s-band image, in the frame of the same image. J2000 position angles may be derived as ϕ(bar, J2000) $= \langle \phi \rangle$(bar)+0°.58; Column 6: mean FWHM of stellar profile in pixels (1 pixel $= 0''.447$) on image; Column 7: range in arcsecs used to get $\langle q \rangle$ and $\langle \phi \rangle$; Column 8: bandpass used for orientation parameters, often a deeper B-band image, available mainly from the OSUBGS, NED, or our unpublished image library. "Opt" means based on several optical filters, "kin" means based partly on kinematic parameters as well.
[a] Orientation parameters from Buta et al. (1998).

understanding of galaxy evolution because a close connection between bars and spirals should manifest itself in the fractions of such features seen at high z.

Observationally, one way to evaluate these ideas is to use near-infrared K_s-band images to infer the gravitational potential due to the dominant stellar backbone of galaxies. With such potentials, we can derive the relative importance of tangential forces due to bars and spirals. Near-infrared imaging is a necessity because optical images are confused by dust and star formation, whereas the K_s-band emphasizes the mass distribution in the old disk (e.g., Block & Wainscoat 1991; Regan & Elmegreen 1997; Block et al. 1999).

In a recent study, Block et al. (2004) analyzed 2.2 μm images of 17 galaxies covering a range of bar strengths and Hubble types. A Fourier-based technique was used to separate the bars from their associated spirals and derive separate maximum relative torques (Buta et al. 2003). The bar and spiral strengths, Q_b and Q_s, are derived from the maximum ratio of the tangential force to the mean background radial force (Combes & Sanders 1981), as obtained after a Fourier decomposition of the galaxy image. To separate the bar and spiral arm components, the empirical fact that the Fourier amplitudes due to the bar increase with radius to a maximum in the same way as they decline past the maximum was used (the "symmetry assumption"). Alternatively, some Fourier profiles can be fitted with one or more Gaussian components (Buta et al. 2005). With such representations, the bar can be extrapolated into the spiral region, and removed from the image. The net result is a "bar+disk" image and a "spiral+disk" image having the same total flux and identical $m = 0$ backgrounds. These separated images can then be analyzed for maximum relative torques due to the nonaxisymmetric features.

In Block et al. (2004), the sample was small and appeared to show a correlation between bar strength Q_b and spiral strength Q_s for galaxies having $Q_b > 0.3$. A hint of the same correlation was also found by Buta et al. (2005) based on more than 100 galaxies in the Ohio State University Bright Galaxy Survey (OSUBGS; Eskridge et al. 2002). No galaxies in either study were found to have $Q_b > 0.6$ and $Q_s < 0.2$. The finding of such galaxies would seriously challenge the idea that bars in general drive spirals.

In this paper, we complement the Block et al. (2004) study by analyzing maximum relative torque strengths in 23 additional barred galaxies of relatively normal morphology and high luminosity. The main selection criterion was bar contrast, and we tried to include bars that were likely to turn out excessively strong when the near-IR image is converted into a gravitational potential. Because the new sample is not statistical in nature, we cannot determine an average bar driving strength for normal galaxies over the type range we have considered. Instead, our goal is to determine if bars drive spirals at all, even if only in a single case. For this we needed a highly selected sample, such as the one we chose, to focus on the most important physical processes that are involved.

Table 2
Absolute Magnitudes and Angular Sizes

Galaxy	μ_o	$(K_s)^o_T$	$M^o_{K_s}$	M^o_B	$r_o(25)$ ($''$)
1	2	3	4	5	6
NGC 175	33.66	9.21	-24.5	-21.0	65.6
NGC 521	34.21	8.57	-25.6	-21.9	97.1
NGC 613	31.48	7.02	-24.5	-21.0	164.9
NGC 986	32.05	7.77	-24.3	-20.6	116.7
NGC 1300	31.57	7.55	-24.0	-20.8	189.3
NGC 1566	31.30	6.88	-24.4	-21.1	249.5
NGC 4593	32.75	7.98	-24.8	-21.3	116.7
NGC 5101	31.88	7.13	-24.8	-20.7	172.6
NGC 5335	34.00	10.08	-23.9	-20.7	64.1
NGC 5365	32.50	7.89	-24.6	-20.5	92.7
NGC 6221	31.40	7.06	-24.3	-21.6	128.0
NGC 6384	31.94	7.48	-24.5	-21.3	202.8
NGC 6782	33.61	8.85	-24.8	-21.4	68.7
NGC 6907	33.25	8.28	-25.0	-21.9	106.4
NGC 7155	32.13	8.96	-23.2	-19.2	64.1
NGC 7329	33.17	8.86	-24.3	-21.1	116.7
NGC 7513	31.70	8.94	-22.8	-19.4	99.3
NGC 7552	31.68	7.53	-24.1	-20.5	104.0
NGC 7582	31.64	7.31	-24.3	-20.8	150.4
IC 1438	32.82	9.28	-23.5	-20.4	72.0
IC 4290	34.04	10.31	-23.7	-20.2	49.8
IC 5092	33.18	9.40	-23.8	-20.6	86.5
UGC 10862	31.97	11.66	-20.3	-18.9	86.5

Notes. Column 1: galaxy name; Column 2: Galactic standard of rest (GSR) distance modulus from NED; Column 3: total K_s-band magnitude corrected for Galactic extinction (NED); Column 4: absolute K_s-band magnitude; Column 5: absolute B-band magnitude based on B^o_T from RC3 and the NED distance modulus in Column 2; Column 6: $r_o(25) = D_o/2$ is the radius of the $\mu_B = 25.0$ mag arcsec^{-2} isophote, corrected for Galactic extinction (from RC3).

The observations are described in Section 2, while the images are discussed in Section 3. Our analysis of the images involved two-dimensional decompositions (Section 4), image deprojection, and bar–spiral separation (Section 5), estimates of bar radii (Section 6), followed by relative torque calculations (Section 7). Descriptions of individual galaxies are provided in Section 8. A discussion is provided in section 9 and conclusions in Section 10.

2. OBSERVATIONS

To examine whether there might be weak spirals in the presence of extremely strong bars, we imaged the 23 galaxies in the K-short (K_s) band using the Infrared Imager and Spectrograph (IRIS2) attached to the 3.9 m Anglo-Australian Telescope (AAT). The run took place from 2004 June 28 to July 5. IRIS2 has a 1024×1024 pixel Rockwell HAWAII-1 HgCdTe detector mounted at the AAT's $f/8$ Cassegrain focus, yielding a scale of 0.447 arcsec pixel^{-1} and a field of view of 7.7 arcmin^2. For the larger of our sample galaxies we imaged offset fields for subsequent sky subtraction of the galaxy images, while for the majority of our targets that were small enough we took series of 1 minute images of the galaxy in alternate quadrants of the array. In either case, individual galaxy exposures were sky-subtracted and then combined into the final images, which have total equivalent on-source exposure times of around 1 hr in almost all cases and a spatial resolution of typically 1.5 arcsec (see Table 1 for details). This gave exceptional depth to the images because of our interest in measuring both bar and spiral torque strengths.

The images were calibrated using Two Micron All Sky Survey (2MASS) data (see below), and depending on the size of the galaxy relative to the field of view, reach a level of 22–24 mag arcsec^{-2} in azimuthally averaged profiles. For the subsequent analysis, we cleaned the images of foreground stars and subtracted any residual background, if the field of view was large enough.

3. MORPHOLOGY

Our sample is morphologically diverse and has a range of properties. Tables 1 and 2 summarize some of these properties. Types are either from the de Vaucouleurs Atlas of Galaxies (Buta et al. 2007, hereafter the deVA) or were estimated by RB from available B-band images. These are generally consistent with types listed in the Third Reference Catalogue of Bright Galaxies (RC3; de Vaucouleurs et al. 1991). After standard processing with IRAF[8] routines, all images were placed into the same units as the deVA, mag arcsec^{-2}. The K_s-band images were calibrated using 2MASS photometry within a $14''$ diameter aperture compiled on the NASA/IPAC Extragalactic Database (NED) Web site. The mean absolute blue magnitude is $\langle M^o_B \rangle = -20.7 \pm 0.8$ (s.d.) and the mean absolute K_s-band magnitude is $\langle M_{K_s} \rangle = -24.0 \pm 1.0$ (s.d.). The galaxies are typical high-luminosity systems.

Figures 1–17 show the de Vaucouleurs Atlas-style images of the 23 galaxies. For seven of the galaxies, only the K_s-band images are shown. For the remaining 16 galaxies, optical images were used to derive color index maps, which reveal the star formation and dust distribution in an especially discriminating manner. For several cases, we show the optical image and the color index map on two scales, as well as the K_s-band image. The source of each optical image is indicated in the caption to each figure. These were calibrated using published photoelectric aperture photometry as described in the deVA.

4. MEAN ORIENTATION PARAMETERS AND BULGE–DISK PROPERTIES

To facilitate deprojection of the galaxy images, mean orientation parameters were derived from ellipse fits. The ellipticity and major axis position angle of isophotes at different surface brightness levels were derived by least squares, and means at large radii were taken to represent the tilt of the disk. The derived values are collected in Table 1 as $\langle q \rangle$, the mean disk axis ratio, and $\langle \phi \rangle$, the mean major axis position angle. The table also lists the mean position angle of the bar, the range of radii used for $\langle q \rangle$ and $\langle \phi \rangle$, as well as the full width at half-maximum (FWHM) of the seeing profile.

Deprojection involved rotating the image by $-\langle \phi \rangle$ and stretching it along the x-axis by $1/\langle q \rangle$. However, before we could do this, it was necessary to make some allowance for the shape of the bulge. For this purpose, we used the two-dimensional bulge/disk/bar decomposition technique of Laurikainen et al. (2004) to allow for the likely less flattened shape of the bulge. This uses an exponential disk defined by central surface brightness $\mu_{disk}(0)$ and radial scale length h_r; a spherical Sérsic (1968) bulge model defined by central surface brightness $\mu_{bulge}(0)$, characteristic radius h_b, and radial exponent $\beta = 1/n$, where n is the Sérsic index; and a Ferrers bar defined by maximum

---

Figure 1. K_s-band images of NGC 175 (upper left), NGC 5335 (upper right), NGC 5365 (lower left), and NGC 7155 (lower right). The images are logarithmic in units of mag arcsec^{-2} and the square fields have side lengths 1.′91 for NGC 175 and NGC 5335, 3.′73 for NGC 5365, and 2.′38 for NGC 7155. North is at the top and east is to the left in each frame.

radii a_{bar} and b_{bar}, central surface brightness $\mu_{bar}(0)$, the angle of the bar relative to the line of nodes ϕ_{bar}, and the bar exponent n_{bar}. The derived parameters are listed in Table 3, including the fractional contributions of the bulge and bar to the total luminosity. Figure 18 shows the quality of the decompositions using azimuthally averaged surface brightness profiles. The actual fits were not made to such profiles, but to individual pixels. Generally, it was necessary to fix the bar semimajor axis radius, a_{bar}, to get a stable solution.

The most important parameters in these kinds of solutions are β, h_r, and B/T. The typical uncertainties in these parameters were evaluated using synthetic data by Laurikainen et al. (2005), who showed that the components can be recovered with an accuracy of nearly 5% when a bulge, disk, and bar are fitted simultaneously. Adding extra components beyond these three could change the B/T value further by 5% (Laurikainen et al. 2006). Although additional components, such as nuclear bars, could improve some of our solutions, we have preferred the simpler three-component models since our goal with the decompositions is mainly image deprojection. Nevertheless, it is interesting to examine the properties of the bulges in our sample. Figure 19 shows a graph of Sérsic index n versus the log of the bulge-to-total luminosity ratio. The vertical and horizontal dashed lines show limits considered by Kormendy & Kennicutt

(2004) to distinguish classical bulges from "pseudobulges." Any bulge having $B/T > 0.5$ was considered by them to be a classical bulge. However, galaxies having $B/T < 0.5$ and $n < 2$ were considered most likely to be pseudobulges. In our sample, 15 out of the 23 galaxies fall within this domain. This significant fraction is consistent with the findings of Laurikainen et al. (2007) for a much larger sample.

5. DEPROJECTED IMAGES AND RELATIVE FOURIER INTENSITY AMPLITUDES

In order to derive bar strengths and other properties of the bars in our sample, we need to deproject the images. To eliminate or minimize bulge "deprojection stretch," the artificial stretching of bulge isophotes due to the less flattened shape of the bulge, we first subtracted the bulge model from the total image as a spherical component. Next, the disk was deprojected using IRAF routine IMLINTRAN in the flux-conserving mode, using the adopted orientation parameters in Table 1. The bulge was then added back. In some cases, the assumption of a spherical bulge is not a good approximation, and the process oversubtracts bulge light along the galaxy minor axis. This leads to "decomposition (or spherical bulge) pinch," where the inner isophotes are pinched (rather than extended)
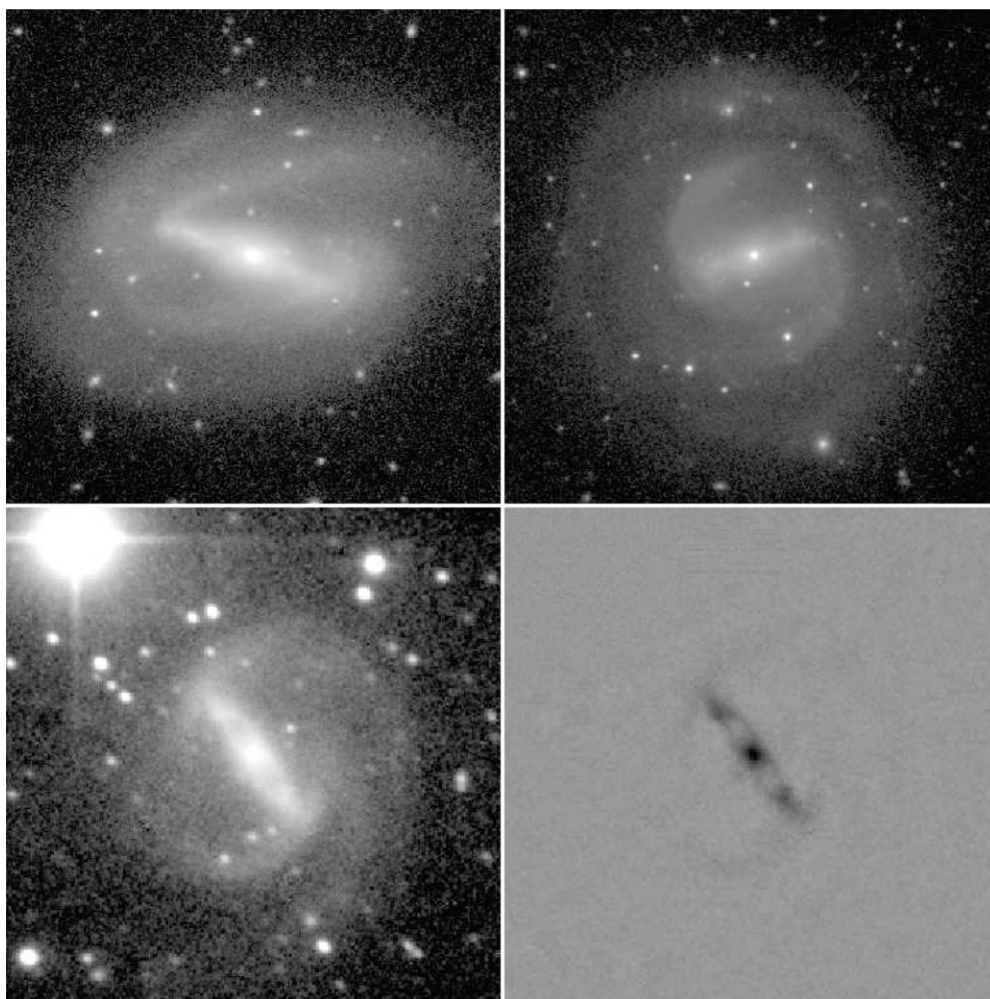
Figure 2. K_s-band images of NGC 7513 (upper left), IC 5092 (upper right), and UGC 10862 (lower left). The images are logarithmic in units of mag arcsec^{-2} and the square fields have side lengths of 2′.98 for NGC 7513 and IC 5092, and 1′.91 for UGC 10862. The lower right image is also of UGC 10862, but is an unsharp-masked image after subtracting a 31 × 31 pixel median smoothed version of the cleaned galaxy image. North is at the top and east is to the left in each frame.

perpendicular to the major axis. Note that both deprojection stretch and decomposition pinch can lead to artificial barlike features, although these are generally weaker than the actual bars and can be easily distinguished.

The relative Fourier intensity amplitudes of the galaxies were derived as a function of radius. In each case, we analyzed the amplitudes in the same manner as in Buta et al. (2003, 2005). To separate the bars from the spirals, in some cases we used the "symmetry assumption" whereby the amplitudes are assumed to decline past a maximum in the same manner as they rose to that maximum. The assumption is based on studies of galaxies where there is little contamination of bar amplitudes by other features. In other cases, we were able to fit one or more Gaussians to the amplitudes to allow for more complex features. The results of these analyses are summarized in Figure 20. Table 4 lists the maximum bar $m = 2$ and 4 relative amplitudes, A_{2b} and A_{4b}, based on the mappings in Figure 20. Table 5 summarizes Gaussian fit parameters for those galaxies where this representation provided a good mapping of the bar. The separated bar and spiral images are shown in Figure 21. No uncertainties are given for the parameters in Tables 4 and 5 because the Fourier profiles are based on averages over many pixels and their statistical uncertainty in the bar regions is very small. Systematic uncertainties in the orientation parameters

due, for example, to inaccurate assumptions about intrinsic disk shapes would generally lead to less than ±10% uncertainty in the values of A_{2b} and A_{4b} for the average low inclination of ≈35° for our sample. Uncertainties in r_{2b} and r_{4b} would also generally be less than ±10%.

6. BAR RADII

Erwin (2005) presented an analysis of bar radii and argued that bar size must be important because it determines how much of a galaxy is impacted by the bar itself. A variety of methods has been proposed to measure this parameter (see, for example, Athanassoula & Misiriotis 2002; Gadotti et al. 2007), but no single technique works consistently for all possible bars. To estimate bar major axis radii, Erwin used ellipse fits to isophotes that gave both lower and upper limits to bar size. The lower limit was taken as the radius of maximum bar ellipticity (see also Marinova & Jogee 2007). Also, if a bar crossed a ring or lens, he used the radius of the ring or lens as an estimate of the bar size. Here, we use another approach: the Fourier mappings of the bars in Figure 20 show that bars do not simply end abruptly but decline smoothly to zero intensity. This suggests that bar radii might be estimated from fractions of the maximum Fourier amplitudes. We ask what fractions well approximate
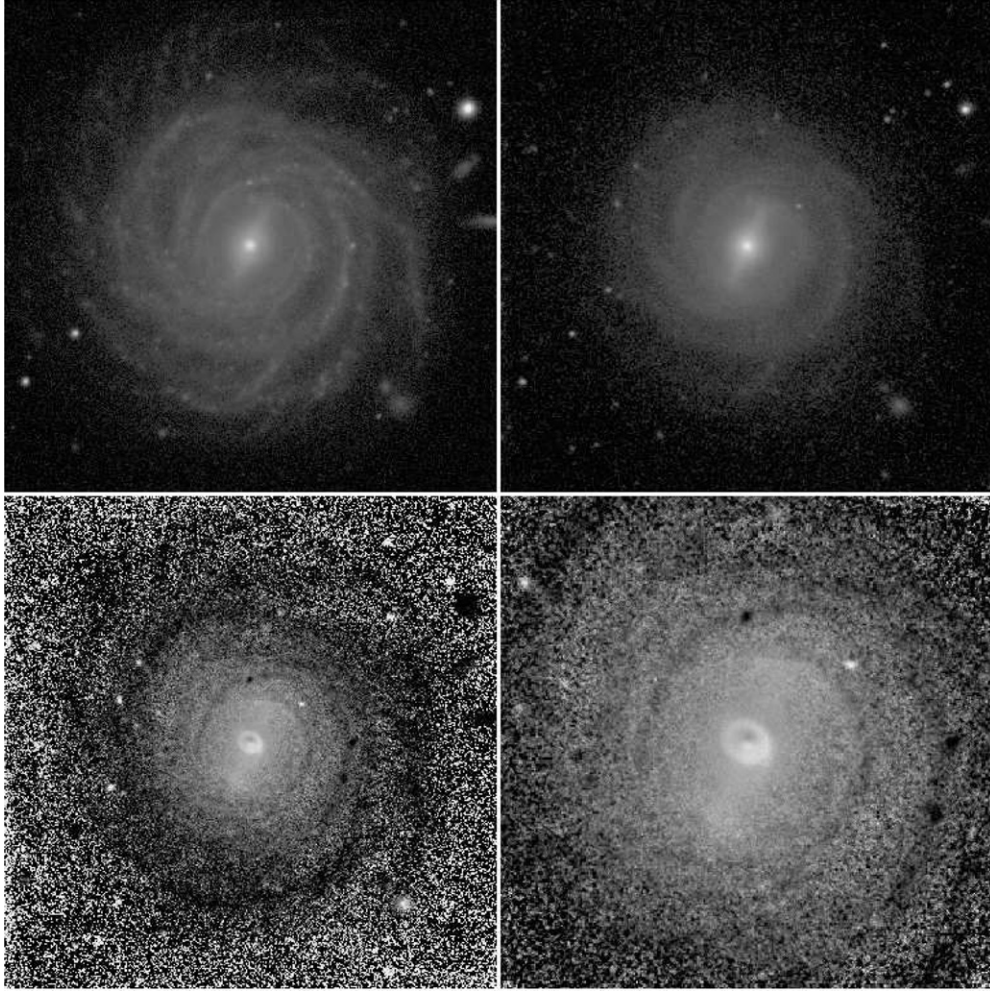
Figure 3. Images of NGC 521. Upper left: *B*-band (Galaz et al. 2006); upper right: K_s-band; lower left: $B - K_s$ color index map; lower right: same as at lower left, at twice the scale. The images are logarithmic in units of mag arcsec^{-2} and the main fields have side lengths of $5'.81$. The color index map for this galaxy and all the others is coded such that blue features are dark and red features are light. North is at the top and east is to the left.

what appears to be the bar radius from visual inspection of our K_s-band images.

Table 6, Column 6 summarizes our visual estimates, considered to be the maximum extents of the features as seen on the images deprojected using our Table 1 orientation parameters. A cursor was placed at each end of the bar on a monitor screen and the coordinates read into a file. The visual bar radius r_{vis} is half the distance between these cursor positions. Figure 22 shows comparisons between r_{vis} and four estimates based on fractions of the maximum Fourier amplitudes A_{2b} and A_{4b} for the bar mappings in Figure 20. These are called "Fourier amplitude fraction radii" r_{FAF} in Figure 22. The bar mappings are well defined for each of our sample galaxies, but often the profile I_2/I_0 involves more extrapolation than I_4/I_0. We found that $r(0.25A_{4b})$ provides a very good approximation to the visual bar radius, matching over a range of radii from $20''$ to $1000''$. However, $r(0.25A_{2b})$ gives radii somewhat larger than the visual bar radii. Instead, we found that $r(0.40A_{2b})$ provided a comparably good match to $r(0.25A_{4b})$, while $r(0.40A_{4b})$ tended to slightly underestimate the bar radius. We adopt $r_{bar} = r(0.25A_{4b})$ as our best estimates, listed in Column 5 of Table 6. Using the NED Galactic standard of rest (GSR) distances, the linear bar radii in Column 7 of Table 6 were derived. The values are comparable to those estimated by Erwin (2005) for galaxies in the type range of our sample.

7. BAR AND SPIRAL TORQUE STRENGTHS

The strengths of the bars and spirals were derived by assuming that the K_s-band light distribution traces the mass distribution. This seems reasonable for bar strength, but one might question whether the near-IR is the best choice for the spiral strength. One could argue that the *B*-band would be best for the spiral because it is more sensitive to the cold component, which would be more reactive to the bar forcing. Nevertheless, the old stellar component is still the best tracer for the spiral arm strength. This would be the amplitude of the actual mode in the stellar disk, and would measure its dynamical significance. Note also that Elmegreen & Elmegreen (1985) showed that the arm–interarm contrast is essentially the same in the *B* and *I* bands in grand design spiral galaxies but is much stronger in *B* than *I* for flocculent galaxies. We expect any bar-driven spirals would be grand design.

As in Block et al. (2004), we used the Cartesian-coordinate method described by Quillen et al. (1994) to derive the gravitational potentials. An exponential density distribution is used for the vertical dimension with a type-dependent scale height based on the work of de Grijs (1998). From these potentials, the radial and tangential forces were derived, and the bar and spiral strengths were estimated from maps of the ratio $F_T(i, j)/F_{0R}(i, j)$, where $F_T(i, j)$ is the tangential force and
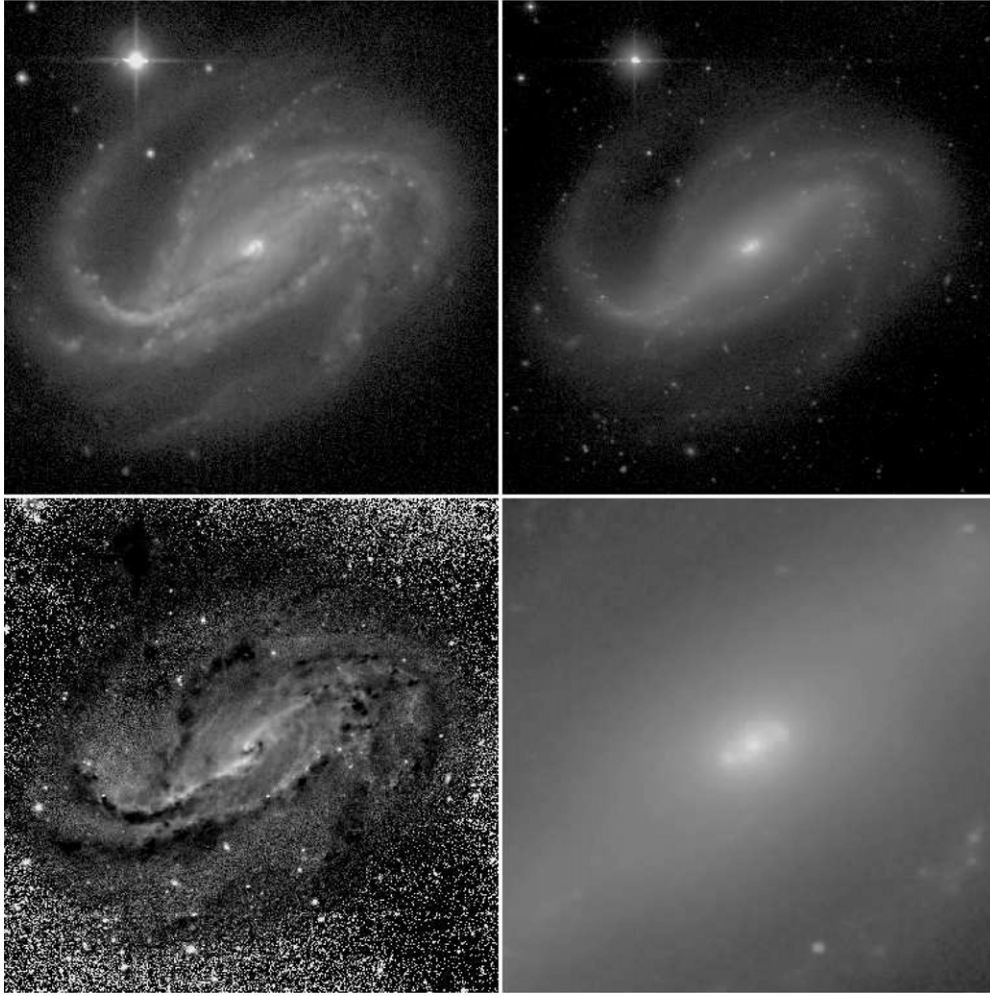
Figure 4. Images of NGC 613. Upper left: *B*-band (Eskridge et al. 2002); upper right: K_s-band; lower left: $B - K_s$ color index map; lower right: same as at upper right, at four times the scale. The images are logarithmic in units of mag arcsec^{-2} and the main fields have side lengths of $5'.30$. North is at the top and east is to the left.

$F_{0R}(i, j)$ is the mean radial (axisymmetric) force, all in the galaxy plane. From a quadrant analysis, the maximum values $Q_T(r) = |F_T(i, j)/F_{0R}(i, j)|_{max}$ were derived as a function of radius. For the bar plus disk images, the maximum of $Q_{Tb}(r)$ is Q_b at radius r_b while for the spiral plus disk images, the maximum of $Q_{Ts}(r)$ is Q_s at radius r_s. The total maximum relative gravitational torque is given by Q_g.

Table 7 summarizes the derived maxima. The uncertainties listed in Table 7 are based on the analysis of Buta et al. (2003) and are estimated as percentages of the values. For Q_s and Q_b, we used 10% for the orientation parameters (meaning $\sigma(Q_b) \approx 0.1 Q_b$ due to this effect, etc.), 10% for the vertical scale height, 4% for the bar extrapolations, and 10% for the spiral extrapolation, for an average sample galaxy inclined by 35°. We also allowed for the scatter in the maxima in each quadrant due to asymmetries in the spiral pattern. Since these uncertainties are largely independent, we added them in quadrature. For the error bars on the spiral contrasts A_{2s} and A_{4s}, we used a similar procedure but without any effect of vertical scale height. The error bars are in any case only indicative. The uncertainties in the Table 7 parameters tend to be larger than those for the Tables 4–6 parameters because Q_b and Q_s involve an uncertain vertical scale height and Q_s, A_{2s}, and A_{4s} are especially sensitive to the extrapolation of the bar. The bar in the present sample with the largest value of Q_b is found in UGC 10862, which has a very

small bulge and near-IR ansae. These conspire to make the bar strong.

Note that if the forcing due to the dark matter halo is more important at larger radii than at smaller radii, then our Q_s values are likely to be more overestimated by ignoring the halo than would our Q_b values, since $r_s \approx 2 r_b$ on average. Our analysis assumes a constant mass-to-light ratio. Buta et al. (2004) shows using a statistical approach how much the effect on Q_b can be for typical high-luminosity galaxies. For galaxies of similar luminosities to those in our AAT sample, the inclusion of a halo reduced Q_b values by 6% on average. Even if the effect on Q_s is twice this amount, it would still be small and have little impact on our results.

The spiral maximum at radius r_s in Table 7 in some cases refers to bright inner arms (e.g., NGC 175), while in others it refers to outer arms (e.g., NGC 521). This depends on how the arms combine with the declining background. In other cases, residual light of an extended oval may contribute to what we call Q_s (e.g., NGC 7155). The bar radius $r(0.25A_{4b})$ from Table 6 correlates well with the Q_b maximum radius r_b in an impartial linear relation of the form $r(0.25A_{4b}) = 1.583(\pm 0.031) r_b$, with a radius-dependent dispersion of $\sigma = 0.082 \, r(0.25A_{4b})$.

As a check on these results, we also derived the potentials (and the resulting Q_b, Q_s values) using the polar grid method of Laurikainen & Salo (2002). Figure 23 shows how well the two

Table 3
Two-Dimensional Decomposition Parameters

Galaxy	$\mu(0)$ Bulge	r_b ($''$)	β	$\mu(0)$ Disk	h_r ($''$)	$a_{\rm bar}$ ($''$)	$b_{\rm bar}$ ($''$)	$\mu(0)$ Bar	$\phi_{\rm bar}$ (deg)	$n_{\rm bar}$	B/T	bar/T
1	2	3	4	5	6	7	8	9	10	11	12	13
NGC 175	14.10	0.99	0.966	17.35	15.2	25.0	5.9	17.62	182.4	0.25	0.074	0.118
NGC 521	13.06	0.81	0.796	17.32	18.8	26.8	8.8	17.30	40.5	3.14	0.133	0.062
NGC 613	12.85	1.82	0.861	17.30	36.8	84.9	22.0	17.96	92.5	0.00	0.144	0.178
NGC 986	13.93	2.78	1.277	18.12	34.5	59.9	23.9	17.11	4.8	2.00	0.137	0.282
NGC1300	12.97	1.03	0.736	18.89	76.8	89.4	30.8	18.47	71.3	1.00	0.099	0.153
NGC1566	10.83	0.15	0.421	16.89	42.5	53.6	21.3	17.30	38.4	1.25	0.129	0.076
NGC4593	8.06	0.00	0.279	18.65	38.1	76.0	24.5	18.35	38.1	0.30	0.345	0.232
NGC5101	11.10	0.16	0.394	18.46	58.2	67.1	28.1	17.41	64.2	0.71	0.280	0.210
NGC5335	14.33	1.34	0.930	18.64	20.1	29.9	8.0	18.02	152.2	0.56	0.188	0.177
NGC5365	11.61	0.59	0.547	19.07	61.3	78.0	28.7	17.99	186.8	2.98	0.480	0.131
NGC6221	11.40	0.43	0.636	16.75	30.5	46.9	11.7	17.39	7.2	0.10	0.091	0.096
NGC6384	11.37	0.04	0.325	17.91	45.9	39.8	17.3	17.02	100.5	4.00	0.118	0.059
NGC6782	11.86	0.28	0.485	18.35	22.0	31.3	14.6	18.16	47.2	0.00	0.408	0.171
NGC6907	13.57	1.25	0.803	17.71	25.1	63.7	25.1	17.71	102.7	2.19	0.127	0.236
NGC7155	12.70	0.85	0.695	18.29	21.0	44.7	15.9	17.51	137.8	2.56	0.356	0.196
NGC7329	12.92	0.82	0.718	18.23	26.2	38.0	11.0	18.40	38.0	0.00	0.211	0.121
NGC7513	15.19	1.12	0.806	17.81	25.6	38.0	7.5	18.28	43.4	0.00	0.033	0.088
NGC7552	10.51	0.19	0.445	18.32	37.3	62.6	20.4	17.45	0.8	0.12	0.384	0.272
NGC7582	7.81	0.02	0.376	17.46	34.4	80.5	24.0	17.96	105.1	0.00	0.178	0.215
IC 1438	13.21	1.26	0.857	19.11	29.0	29.1	19.7	17.98	81.5	0.72	0.325	0.235
IC 4290	14.43	0.64	0.724	19.34	19.7	31.3	8.7	18.46	142.9	0.45	0.141	0.264
IC 5092	9.35	0.00	0.321	18.32	24.5	31.3	8.5	18.22	164.4	0.68	0.050	0.107
UGC10862	17.98	1.70	1.468	19.20	23.5	26.8	7.0	18.76	−36.2	0.49	0.009	0.125

Notes. Column 1: galaxy name; Column 2: bulge central surface brightness (mag arcsec^{-2}); Column 3: bulge characteristic radius; Column 4: Sérsic β parameter; Column 5: disk central surface brightness (mag arcsec^{-2}); Column 6: disk radial scale length; Columns 7 and 8: maximum bar major and minor axis radii; Column 9: bar central surface brightness (mag arcsec^{-2}); Column 10: bar position angle in galaxy plane relative to line of nodes; Column 11: bar exponent; Column 12: bulge-to-total luminosity ratio; Column 13: bar-to-total luminosity ratio.

**Table 4**
Relative Bar Parameters and Fourier Component Radii

Galaxy	A_{2b}	r_{2b} ($''$)	$r_{2b}/r_o(25)$	A_{4b}	r_{4b} ($''$)	$r_{4b}/r_o(25)$
1	2	3	4	5	6	7
NGC 175	0.664	12.5	0.191	0.394	15.5	0.236
NGC 521	0.398	12.5	0.129	0.218	13.5	0.139
NGC 613	0.598	57.5	0.349	0.347	62.5	0.379
NGC 986	0.805	33.5	0.287	0.454	35.5	0.304
NGC1300	0.861	59.5	0.314	0.455	57.5	0.304
NGC1566	0.308	32.5	0.130	0.129	29.5	0.118
NGC4593	0.876	60.5	0.518	0.462	43.5	0.373
NGC5101	0.711	48.5	0.281	0.388	45.5	0.264
NGC5335	1.003	14.5	0.226	0.630	16.5	0.258
NGC5365	0.623	36.5	0.394	0.389	37.5	0.405
NGC6221	0.618	26.5	0.207	0.297	27.5	0.215
NGC6384	0.257	18.5	0.091	0.106	20.5	0.101
NGC6782	0.711	26.5	0.386	0.308	27.5	0.400
NGC6907	0.687	23.5	0.221	0.322	24.5	0.230
NGC7155	0.783	21.5	0.336	0.478	22.5	0.351
NGC7329	0.663	24.5	0.210	0.411	26.5	0.227
NGC7513	0.717	23.5	0.237	0.360	23.5	0.237
NGC7552	1.104	46.5	0.447	0.682	48.5	0.466
NGC7582	0.902	64.5	0.429	0.539	67.5	0.449
IC 1438	0.620	21.5	0.299	0.256	22.5	0.313
IC 4290	0.912	16.5	0.331	0.596	17.5	0.352
IC 5092	0.621	16.5	0.191	0.340	17.5	0.202
UGC 10862	0.722	12.5	0.145	0.440	13.5	0.156

Notes. Column 1: galaxy name; Column 2: maximum relative $m = 2$ Fourier intensity amplitude $A_{2b} = (I_2/I_0)_{\rm max}$ of the bar, in the K_s band; Column 3: radius of A_{2b}; Column 4: the ratio of r_{2b} to the radius of the corrected isophotal diameter $D_o(25)$ from RC3 (Table 2); Columns 5–7: same parameters for $m = 4$.

methods agree for our 23 galaxies. In general, the agreement is good but we find small average offsets: for Q_b, the Cartesian values are on average larger than the polar grid values by 0.038 while for Q_s they are larger by 0.033. These differences are not due to the integration method (Cartesian versus polar grid) but are likely due to slightly different treatments of the bulge and the vertical scale height in the two independent sets of programs. However, because the differences are virtually the same, they will have little or no effect on a possible correlation between Q_b and Q_s.

Figure 24 compares Q_b and the bar contrast parameters A_{2b} and A_{4b} with the relative radii of these maximum parameters. The radii are normalized to $r_o(25) = D_o/2$, where D_o is the extinction-corrected isophotal diameter at $\mu_B = 25.0$ mag arcsec^{-2} from RC3. The values of A_{2b} and A_{4b} (and r_{2b} and r_{4b}) are from Table 4, and are based on the same mappings (Figure 20) used to derive Q_b. There is little apparent correlation between Q_b and $r_b/r_o(25)$, but A_{2b} and A_{4b} do show some correlation. The correlation between A_{2b} and $r_{2b}/r(25)$ for this sample has already been discussed by Elmegreen et al. (2007). These authors argue that this contrast correlation, in addition to a correlation with central density, implies that bars grow in both length and contrast over a Hubble time through angular momentum transfer to the disk and halo.

Table 8 summarizes the mean values of several parameters from our analysis for those galaxies where single or double Gaussians well-represented the relative Fourier profiles. Buta et al. (2006) showed that bars fitted by double Gaussians were stronger than those fitted with single Gaussians. In the present sample, the single and double Gaussian bars have the same
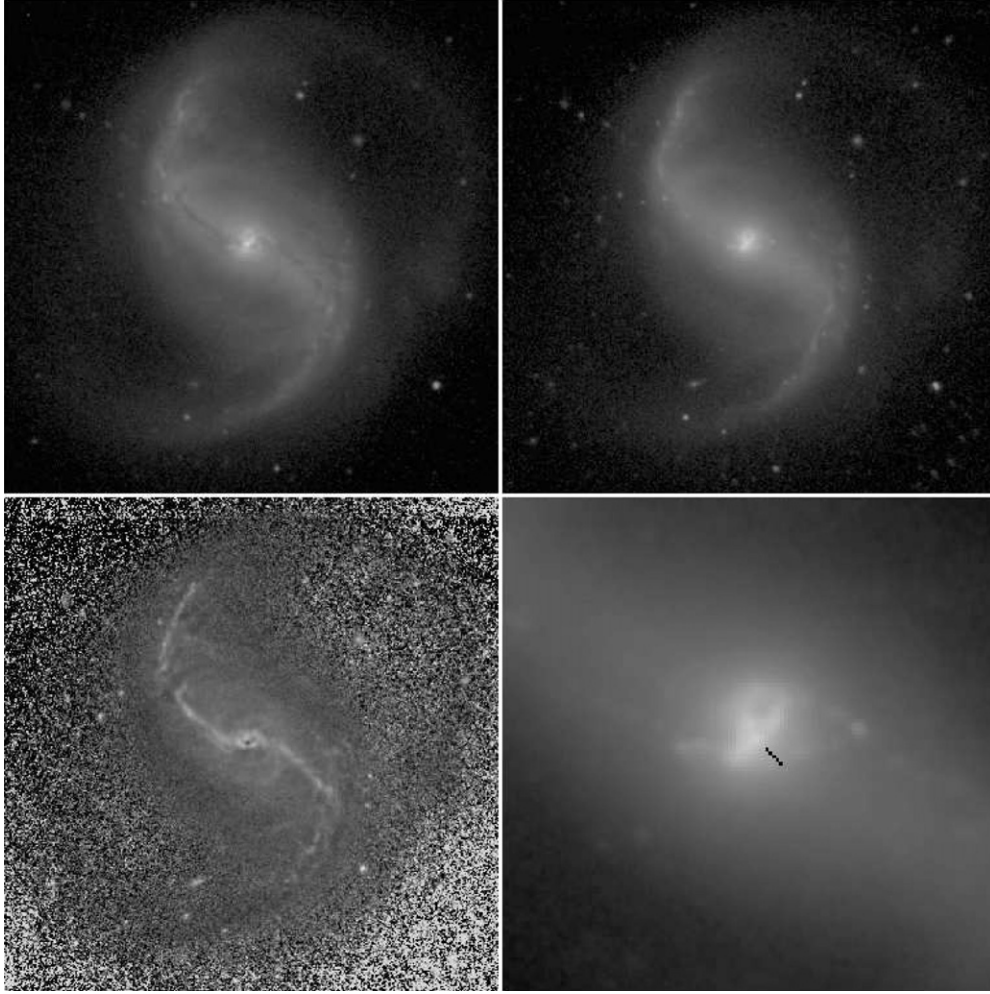
Figure 5. Images of NGC 986. Upper left: R-band (Hameed & Devereaux [1999]); upper right: K_s-band; lower left: $R - K_s$ color index map; lower right: same as at upper right, at four times the scale. The images are logarithmic in units of mag arcsec^{-2} and the main fields have side lengths of $3\rlap{.}'73$. North is at the top and east is to the left. In the lower right frame, the short dark line points to the feature recognized as the nucleus in our analysis.

relative torque strength on average, while the contrasts are higher for the double Gaussian features. The double Gaussian features also have higher average values of r_{bar}/h_r, bulge-to-total luminosity ratio, and Sérsic index, which may conspire to make the torque strengths similar to those of the single Gaussian bars.

Laurikainen et al. ([2007]) noted that strong bars with thin and thick components have double-peaked profiles in all Fourier modes. But in galaxies where only the $m = 2$ profile (not the higher Fourier modes) of the bar is double-peaked, the amplitude is most probably contaminated by an inner or outer oval/lens.

One issue we can examine with our new data set is the steepness with which the bar declines near its ends. More evolved, stronger bars should have more steeply falling amplitude profiles because their orbits are pushed right up against the resonances. Noncircular orbits and random stellar motions should broaden the bar's edge. We examine this issue using $Q_{Tb}(r)$ forcing profiles, rather than the Fourier luminosity profiles, because these most reliably trace how rapidly the significance of the bar declines. Only the maxima Q_b of the $Q_{Tb}(r)$ profiles are compiled in Table 7, which also gives $r_b = r(Q_b)$. To remove the effects of distance and scale, we normalize the profiles as $S_{Tb} = Q_{Tb}(r)/Q_b$ vs. $\rho = r/r_b$. Figure 25(a) shows the normalized profiles for IC 1438 and IC 4290, the former having $Q_b = 0.12$ and the latter having $Q_b = 0.52$. The curves show

that the strong bar in IC 4290 has the more steeply declining normalized bar torque profile. We measure the steepness of the bar on its declining edge as the slope $S_b = dS_{Tb}/d\rho$ at the point on the profile where S_{Tb} drops to 0.5 (the filled circles in Figure 25(a)). Figure 25(b) shows that, for our 23 galaxies, S_b generally declines with increasing Q_b, although with considerable scatter. On average, the bar torque profiles do decline more steeply past the end of the bar for stronger bars than for weaker bars, for our small sample.

We also define the relative bar-end drop-off distance as

$$f_b = \frac{(r(0.25Q_b) - r(0.75Q_b))}{r_b},$$

where $r(0.75Q_b)$ is the radius where the $Q_{Tb}(r)$ profile drops to 75% of the maximum value, $r(0.25Q_b)$ is the radius where the $Q_{Tb}(r)$ profile drops to 25% of its maximum value, and r_b is again the radius of the maximum from Table 7. This fraction is plotted versus Q_b in Figure 25(c). The plot shows that like S_b, f_b declines slightly with increasing Q_b, which is also consistent with the stronger bars having a steeper decline past the maximum, relative to the Q_b bar radius.

We also examined whether S_b and f_b correlated with any other quantities, such as $r_b/r_o(25)$, r_b/h_r, M_B, and T, but no other significant correlations were found.
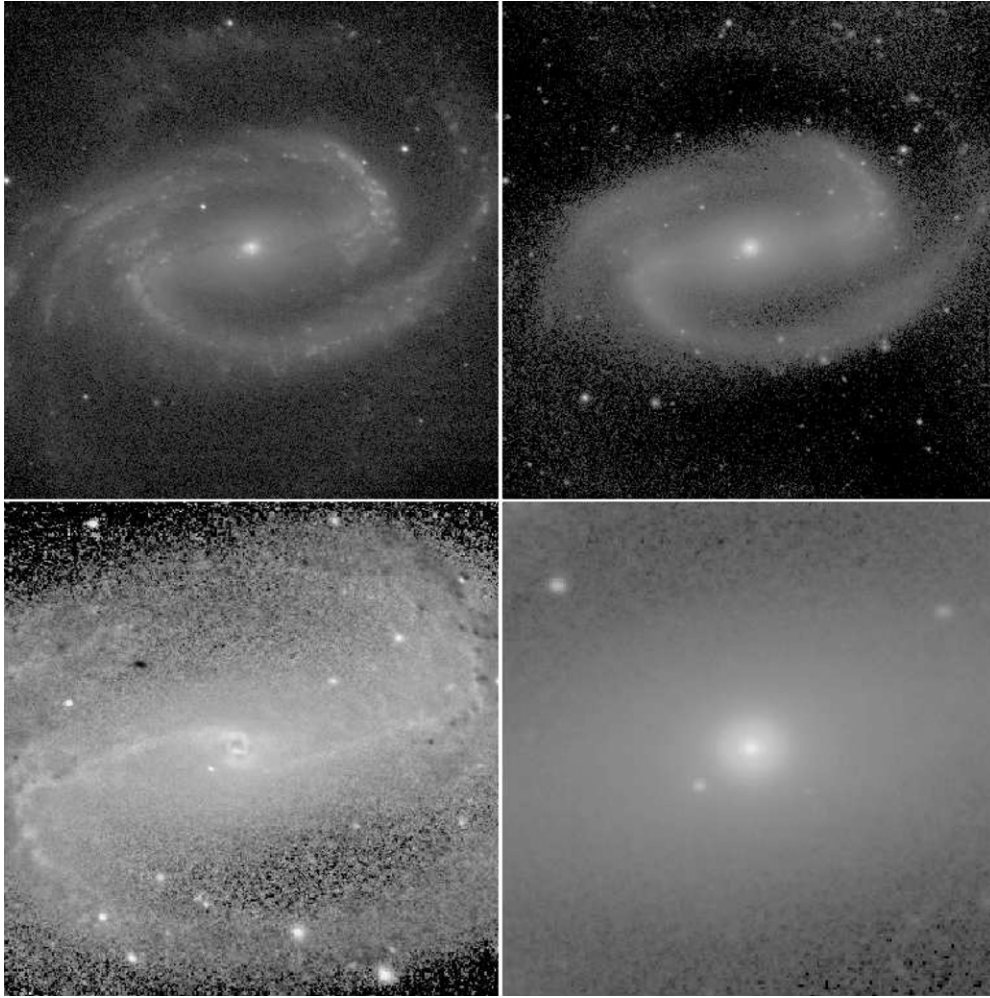
Figure 6. Images of NGC 1300. Upper left: *B*-band (R. B. Tully, deVA); upper right: K_s-band; lower left: $B - K_s$ color index map at twice the scale of the upper panels; lower right: same as at upper right, at four times the scale. The images are logarithmic in units of mag arcsec^{-2} and the main fields have side lengths of $3'.73$. North is at the top and east is to the left.

8. DESCRIPTION OF INDIVIDUAL GALAXIES

In this section, bar and spiral strength classes are defined as in Buta & Block (2001) and Buta et al. (2005). Class 0 refers to values less than 0.05, class 1 to values ranging from 0.05 to 0.15, class 2 to values 0.15–0.25, etc.

NGC 175. The near-IR morphology of this galaxy (Figure 1) is almost as structured as its blue light morphology in the Hubble Atlas (Sandage 1961). The inner pseudoring has a diameter of 13.6 kpc, comparable to the average for SB inner rings as derived by de Vaucouleurs & Buta (1980), after adjustment for distance scale. The two-dimensional decomposition gave an exponential bulge including 7.4% of the total luminosity. Figures 20 and 21 show that a single Gaussian component well represents the bar. The removal of this bar representation from the image leaves an elongated inner pseudoring that is slightly misaligned with the bar axis. This suggests that the bar and spiral in this case have a different pattern speed, because alignment is the normal rule for inner rings and pseudorings (Buta 1995). The bar is strong and corresponds to bar class 4, while the spiral class is 2.

NGC 521. Figure 3 shows that the *B*- and K_s-band morphologies are similar except that the outermost spiral features are much weaker in K_s. The bar is enveloped by a conspicuous inner pseudoring in the *B*-band that is much weaker in K_s. The deprojected K_s-band diameter of the ring is 14.9 kpc using the

NED GSR distance of 69.6 Mpc. The deprojected axis ratio is 0.95. In addition to the inner pseudoring, the $B - K_s$ color index map in Figure 3 shows a very well-defined, red nuclear ring. In the *B*-band, the ring is a clear dust feature with no recent star formation evident. A visual mapping of the ring in the color index map gives an axis ratio of 0.82 and a diameter of $15''.4$ or 5.2 kpc, unusually large for a nuclear ring. These are close to the face-on values since the galaxy is only slightly inclined. There are no prominent bar dust lanes.

The fitted bulge model is nearly exponential, and corresponds to a Sérsic index of $n = 1.26$. A single Gaussian component well represents the K_s-band relative Fourier intensity amplitudes, with only a slight departure of the peak $m = 2$ amplitude from the Gaussian fit. In spite of the conspicuousness of the bar, it is a relatively weak feature and has a bar class of 1 and a "Q_b family" (Buta et al. 2005) of only SAB. The spiral class is 1.

NGC 613. A complicated object with at least five spiral arms, all of which are still prominent in the K_s-band. After deprojection, the inner pseudoring has an axis ratio of 0.67 and a diameter of $2'.46$ or 6.3 kpc, and is aligned almost exactly parallel to the bar. The $B - K_s$ color index map in Figure 4 shows strong leading dust lanes in the bar. The *B*-band image shows a small spiral in the center that in the K_s-band is either a nuclear ansae bar or a nuclear ring highly elongated along the main bar (Böker et al. 2008). This feature is shown in the lower
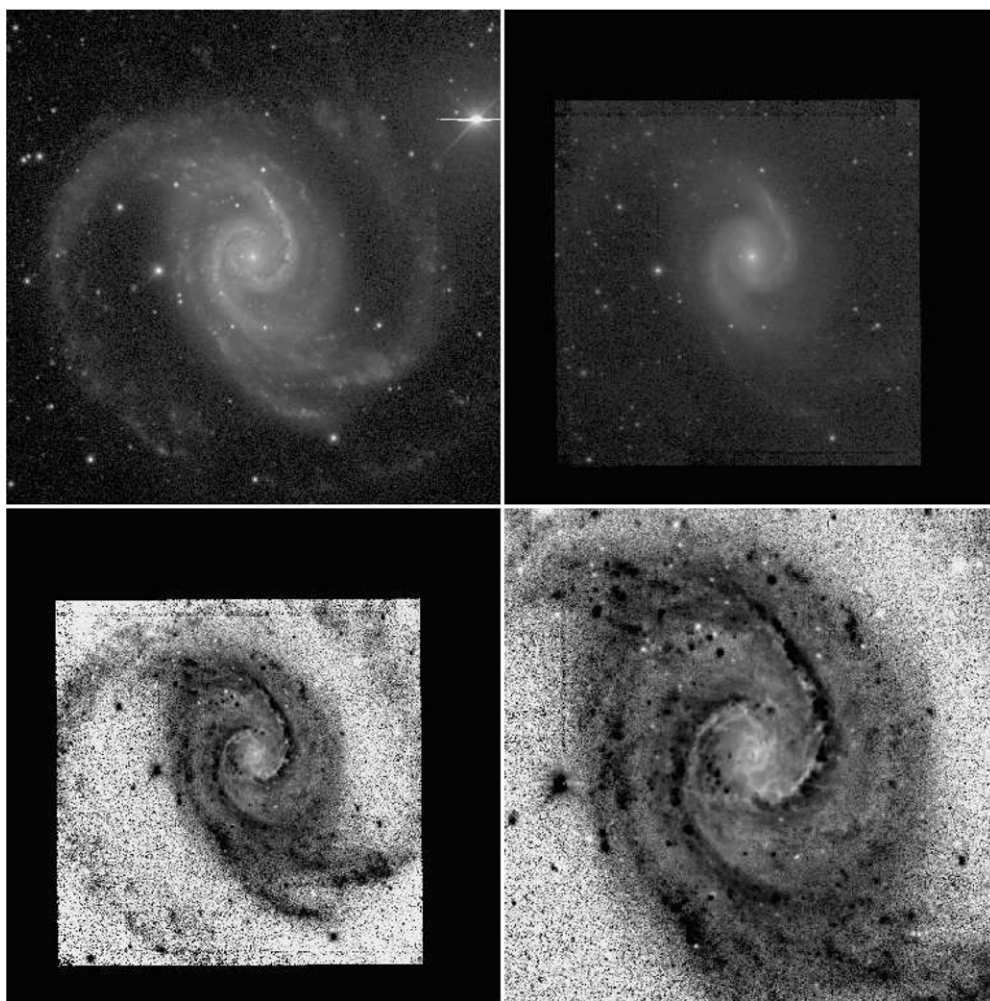
Figure 7. Images of NGC 1566. Upper left: B-band (Kennicutt et al. 2003); upper right: K_s-band; lower left: $B - K_s$ color index map; lower right: same as at lower left, at twice the scale. The images are logarithmic in units of mag arcsec^{-2} and on the same scale. The B-band field has a side length of $10.\!'15$. North is at the top and east is to the left.

right panel of Figure 4. The projected diameter of the feature is $9.\!''8$ (0.94 kpc). Peeples & Martini (2006) show a structure map of this same area, illustrating fine details of the dust distribution.

The decomposition yielded a nearly exponential bulge with a flux contribution of 14.4%. However, this is probably an overestimate due to the nuclear bar/ring. The relative Fourier intensities show a bar that is not easily interpreted in terms of single or double Gaussians. The double-humped profiles in Figure 20 are a symmetry-assumption mapping that was needed to get the maximum extent of the bar but which fails to account for the significant asymmetry in that feature that is apparent in the spiral plus disk image in Figure 21. After separation, we find that NGC 613 is bar class 4 and spiral class 3.

NGC 986. This galaxy is characterized by apparently strong bar and spiral patterns. The bar and spiral are closely connected, such that the bar smoothly changes into the spiral. The $R - K_s$ color index map (Figure 5) shows very well-defined dust lanes on the leading edges of the bar as well as strong red features in the inner parts of the spiral arms. The nuclear region is complicated in both R and K_s, and appears to include a small nuclear dust ring $9.\!''6$ (1.2 kpc) in projected diameter. The short black line in the lower right panel of Figure 5 points to the object we have taken to be the nucleus of the galaxy. From the color index map, this object has blue colors.

The two-dimensional decomposition gave a large value of β, 1.277, and a rather large value of bulge-to-total luminosity ratio, 13.7%. The bulge region of NGC 986 is not very smooth and it is likely that these values are unreliable. Bar–spiral separation is also not clean in NGC 986 because the bar blends so smoothly with the spiral. In our final analysis, we assumed what little bulge might be present in this galaxy to be as flat as the disk. The bar mapping in Figure 20 does a reasonable job of separation. Conversion of the separated images to a potential gives a bar class of 4 and a spiral class of 5. By this measure, NGC 986 has the strongest spiral of the sample.

Kohno et al. (2008) recently observed NGC 986 in CO(3-2), and found the galaxy's bar to be rich in dense molecular gas. These authors have suggested that the complex central region of the galaxy is in a growing phase, being fueled by the significant gas in the bar.

NGC 1300. The bar and spiral pattern in this galaxy are strong and well defined (Figure 6). The $B - K_s$ color index map reveals strong leading dust lanes in the bar. Buta et al. (2007) show a $B-I$ color index map that reveals a small blue nuclear ring. In the K_s-band, this feature is a smooth, almost circular lenslike feature of projected diameter $9.\!''4$ (0.9 kpc; see Figure 6, lower right panel). The two-dimensional decomposition gave a nearly exponential bulge including 9.9% of the total K_s-band luminosity.
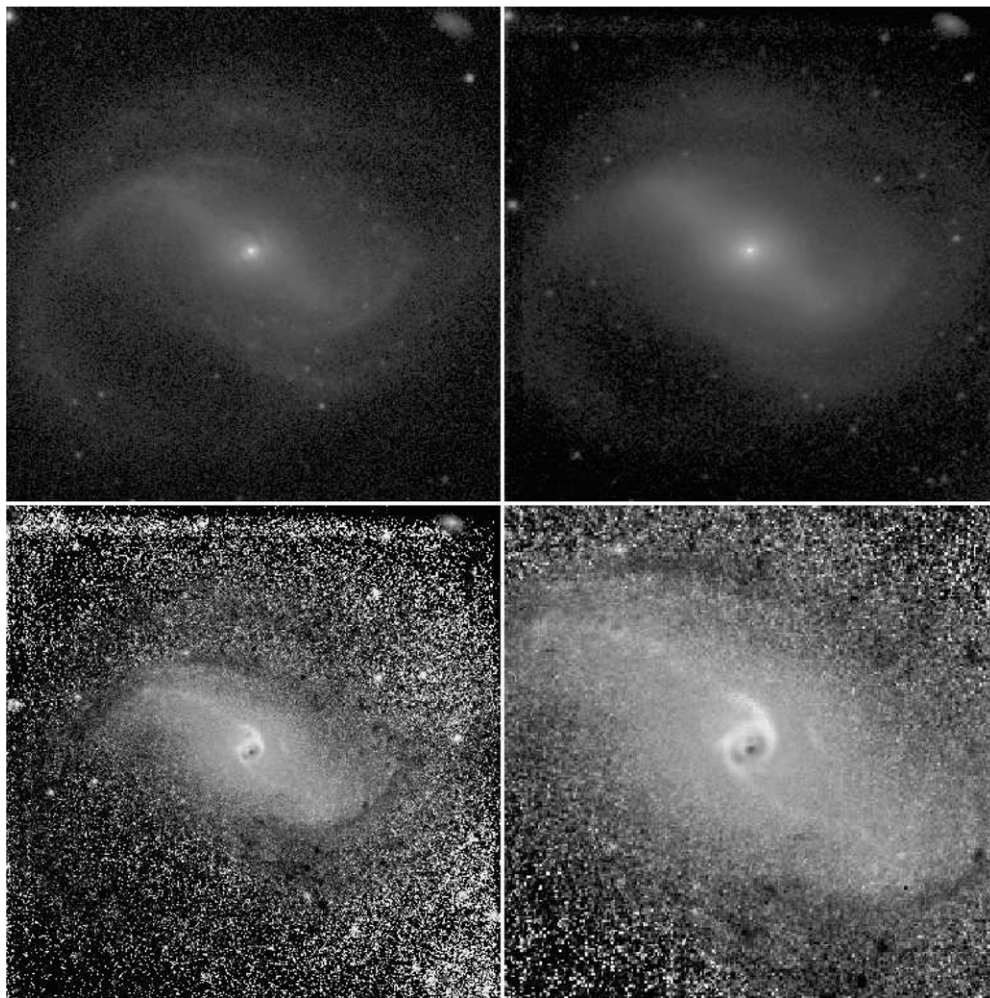
Figure 8. Images of NGC 4593. Upper left: *B*-band (Eskridge et al. 2002); upper right: K_s-band; lower left: $B - K_s$ color index map; lower right: same as at lower left, at twice the scale. The images are logarithmic in units of mag arcsec^{-2} and the main fields have side lengths of 3.′73. North is at the top and east is to the left.

The bar representation in Figure 20 is a double-Gaussian mapping that is somewhat uncertain. Figure 21 shows that this mapping does a reasonable job of separating the bar from the spiral. With this separation, the galaxy is bar class 5 and spiral class 2.

NGC 1566. The bar lies inside the inner termination points of the bright spiral (Figure 7), as first shown by Hackwell & Schweizer (1983). The two-dimensional decomposition (Figure 18) gave a bulge having Sérsic index $n = 2.4$ and including 12.9% of the total K_s luminosity. The relative Fourier amplitudes in Figure 20 show an asymmetric $m = 2$ profile inside $r = 40''$ that is associated with the inner bar. The symmetry assumption could be applied to all higher order terms but $m = 2$. Although within the broad definitions of the classes this galaxy is both bar and spiral class 2, it is the second case in our sample where the spiral is stronger than the bar.

NGC 4593. Except for the obvious leading bar dust lanes and a nuclear dust ring, the *B*- and K_s-band images of this galaxy are very similar. The nuclear dust ring seen in the $B - K_s$ color index map has a projected diameter of 11.′′0 (1.9 kpc). The two-dimensional decomposition shown in Figure 18 has a Sérsic index of 3.6 and a bulge-to-total K_s-band luminosity ratio of 34.5%, providing a possible classical bulge. The relative Fourier intensity amplitudes shown in Figure 20 are well fitted by double Gaussians in all terms; this representation does a reasonable job

with the bar–spiral separation (Figure 21). With these images, the bar class is 3 and the spiral class is 1.

NGC 5101. The *B*- and K_s-band images are similar, but the exceptional image quality on the K_s-band image reveals short spiral arcs around the ends of the bar (see the lower left panel of Figure 9). The $B - K_s$ color index map reveals only a weak trace of leading bar dust lanes, in addition to a tightly wrapped pattern of spiral arms that wrap around the bar and which have slightly enhanced blue colors.

The two-dimensional decomposition gave a Sérsic index of 2.5 and a bulge contribution of 28%. The relative Fourier amplitudes of the bar are well represented by double Gaussians to $m = 12$, while for $m > 12$, a single Gaussian describes these amplitudes. In the K_s-band, the spiral structure in NGC 5101 is very weak. The derived bar class is 2 and the spiral class is 0.

NGC 5335. The morphology is characterized by a strong apparent bar and a conspicuous inner ring that is weak near its projected major axis (Figure 1). A visual mapping of the ring in the deprojected image in Figure 21 gives an axis ratio of 0.89 and an alignment nearly perpendicular to the bar, very unusual for an SB inner ring (Buta 1995). The ring also has an enormous linear diameter, 16.8 kpc (54.′′8), also unusual for such features (de Vaucouleurs & Buta 1980).

The two-dimensional decomposition gave an exponential bulge and a bulge-to-total luminosity ratio of 18.8%. The bar is

Table 5
Gaussian Fourier Components for 23 Galaxies

Galaxy	A_{2i}	A_{4i}	A_{6i}	A_{8i}	r_{2i}	r_{4i}	r_{6i}	r_{8i}	σ_{2i}	σ_{4i}	σ_{6i}	σ_{8i}
1	2	3	4	5	6	7	8	9	10	11	12	13
NGC 175	0.66	0.40	0.23	0.14	12.5	15.1	15.4	15.3	5.9	5.0	4.5	4.0
NGC 521	0.40	0.22	0.14	0.09	12.8	13.1	13.4	13.5	5.7	4.6	4.2	3.4
NGC 1300-1	0.34	0.46	0.28	0.16	34.3	57.3	58.8	59.1	11.2	16.2	12.2	12.8
NGC 1300-2	0.84	0.00	0.00	0.00	62.4	0.0	0.0	0.0	20.3	0.0	0.0	0.0
NGC 4593-1	0.69	0.44	0.24	0.14	37.3	41.0	40.4	40.1	14.4	11.9	9.5	8.1
NGC 4593-2	0.76	0.23	0.17	0.13	67.1	62.4	59.1	58.3	14.7	9.5	10.1	8.6
NGC 5101-1	0.62	0.22	0.13	0.17	36.3	31.7	33.4	43.7	12.6	7.0	6.0	8.7
NGC 5101-2	0.39	0.37	0.25	0.00	52.7	47.2	47.2	0.0	6.7	8.2	6.7	0.0
NGC 5335-1	1.00	0.61	0.36	0.25	14.9	16.0	16.2	18.5	5.7	4.5	3.7	4.2
NGC 5335-2	0.35	0.25	0.19	0.06	23.7	22.3	22.8	25.7	2.6	2.6	3.5	1.2
NGC 5365-1	0.11	0.01	0.08	0.04	25.3	25.1	27.0	27.0	3.9	3.8	4.6	4.7
NGC 5365-2	0.62	0.39	0.25	0.16	36.8	37.8	40.5	41.2	11.3	10.1	7.2	8.0
NGC 6384	0.26	0.11	0.06	0.03	18.4	20.6	20.1	19.9	6.6	4.0	3.3	3.3
NGC 6782-1	0.12	0.09	0.06	0.03	13.5	14.1	17.4	17.5	2.2	3.5	3.0	2.9
NGC 6782-2	0.71	0.31	0.15	0.07	26.5	27.3	28.3	28.4	8.5	6.6	4.4	4.2
NGC 7155	0.78	0.48	0.29	0.18	21.4	22.2	22.3	22.9	7.9	6.4	6.1	6.1
NGC 7329	0.66	0.41	0.25	0.13	24.6	26.3	27.1	28.1	10.9	6.9	5.9	5.4
NGC 7513-1	0.57	0.24	0.11	0.12	19.5	20.3	22.2	24.0	9.2	5.6	4.2	5.4
NGC 7513-2	0.49	0.34	0.19	0.11	37.0	34.3	32.1	35.3	10.2	8.7	9.5	7.3
NGC 7552-1	0.00	0.18	0.23	0.18	0.0	33.2	34.9	36.5	0.0	9.0	7.8	7.4
NGC 7552-2	0.00	0.66	0.47	0.31	0.0	52.2	53.2	53.2	0.0	16.7	10.7	9.2
NGC 7582-1	0.21	0.21	0.22	0.08	41.5	42.5	54.8	46.3	12.4	7.9	21.1	10.6
NGC 7582-2	0.87	0.54	0.18	0.23	67.6	67.4	70.3	69.0	20.9	15.1	8.0	9.8
IC 1438-1	0.62	0.26	0.12	0.05	21.7	22.2	22.3	21.9	5.9	4.6	3.9	3.4
IC 1438-2	0.11	0.03	0.01	0.01	10.2	12.9	16.6	12.0	2.8	3.1	5.7	3.8
IC 4290-1	0.82	0.58	0.29	0.21	13.8	16.5	16.2	16.5	6.8	4.5	3.7	3.4
IC 4290-2	0.33	0.27	0.26	0.16	22.3	24.2	22.2	22.7	4.8	3.1	4.1	3.7
IC 5092	0.62	0.34	0.20	0.11	16.5	17.6	17.8	18.1	8.0	5.9	5.6	6.0
UGC 10862	0.72	0.44	0.27	0.17	12.9	13.2	14.0	14.4	5.5	3.5	3.2	3.0

Notes. Column 1: galaxy name. If a double Gaussian was fitted to the I_m/I_0 profiles, the first Gaussian is listed as "−1" while the second is "−2." Columns 2–5: Gaussian relative amplitudes A_{mi} for $m = 2, 4, 6$, and 8. The index $i = 1$ for a single Gaussian fit, and 1 and 2 for a double Gaussian fit. For a double Gaussian fit, A_{m1} is listed on the first line and A_{m2} is listed on the second line for a given galaxy. Columns 6–9: mean radii r_{mi} in arcseconds. Columns 10–13: Gaussian width σ_{mi} in arcseconds.

Table 6
Bar Radii

Galaxy	$r(0.4A_{2b})$ ('')	$r(0.25A_{2b})$ ('')	$r(0.4A_{4b})$ ('')	$r(0.25A_{4b})$ ('')	$r(vis)$ ('')	$r(0.25A_{4b})$ (kpc)
1	2	3	4	5	6	7
NGC 175	20.5	22.4	21.9	23.4	22.9	6.1
NGC 521	20.6	22.4	19.4	20.8	20.4	7.0
NGC 613	79.1	81.7	75.1	78.7	79.4	7.6
NGC 986	53.9	57.6	51.3	54.6	59.3	6.8
NGC 1300	89.5	95.8	79.3	84.3	83.3	8.4
NGC 1566	40.2	41.3	39.6	42.6	40.2	3.8
NGC 4593	85.6	90.5	70.2	74.2	78.6	12.8
NGC 5101	60.8	63.3	58.0	60.6	68.4	7.0
NGC 5335	25.8	27.1	24.8	25.9	27.1	7.9
NGC 5365	52.1	55.7	51.5	54.6	55.3	8.4
NGC 6221	42.3	44.6	39.8	42.1	40.6	3.9
NGC 6384	27.3	29.4	26.0	27.3	25.6	3.2
NGC 6782	38.0	40.6	36.2	38.2	44.4	9.7
NGC 6907	32.5	34.9	32.3	34.7	33.9	7.5
NGC 7155	32.0	34.5	30.8	32.8	34.3	4.2
NGC 7329	39.3	42.7	35.7	37.9	37.9	7.9
NGC 7513	47.6	51.4	45.7	48.5	45.2	5.1
NGC 7552	77.1	81.0	74.4	79.7	68.8	8.4
NGC 7582	95.3	101.9	87.8	92.6	90.9	9.6
IC 1438	29.7	31.5	28.4	29.9	29.3	5.3
IC 4290	26.4	28.3	26.7	28.0	28.7	8.7
IC 5092	27.3	29.8	25.5	27.3	26.6	5.7
UGC 10862	20.3	22.0	18.0	19.1	21.9	2.3

Notes. Column 1: galaxy name; Column 2: radius at which the bar $m = 2$ amplitude is $0.4A_{2b}$; Column 3: radius at which the bar $m = 2$ amplitude is $0.25A_{2b}$; Column 4: radius at which the bar $m = 4$ amplitude is $0.4A_{4b}$; Column 5: radius at which the bar $m = 4$ amplitude is $0.25A_{4b}$; Column 6: visual bar radius (arcsec); Column 7: Column 5 bar radius (kpc).
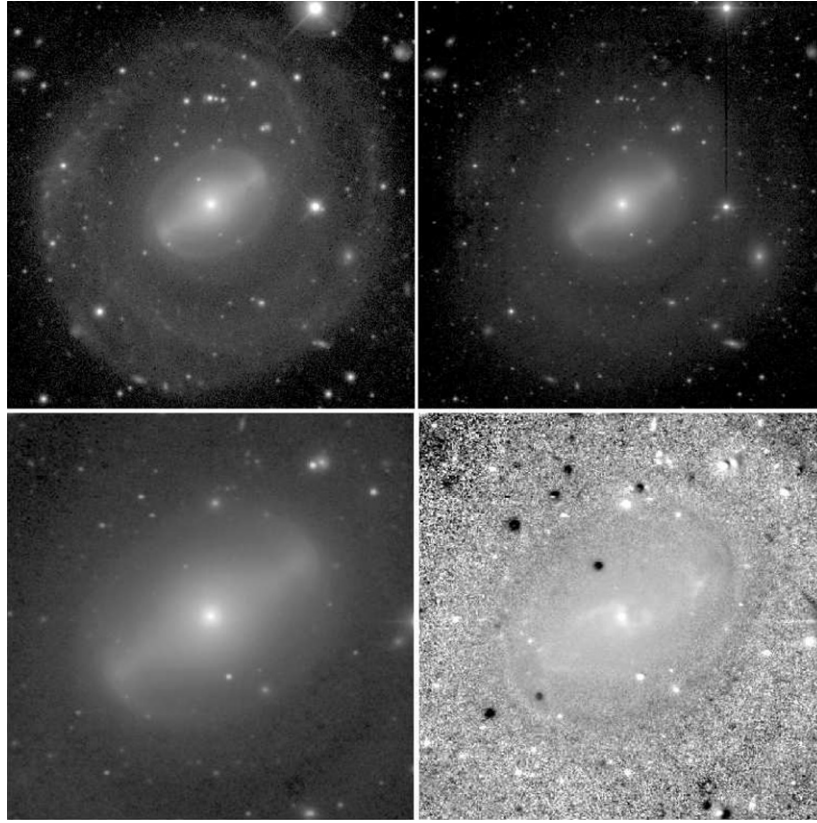
Figure 9. Images of NGC 5101. Upper left: *B*-band (Eskridge et al. 2002); upper right: K_s-band; lower left: same as at upper right, at twice the scale; lower right: $B - K_s$ color index map, also at twice the scale of the upper panels. The images are logarithmic in units of mag arcsec^{-2} and the main fields have side lengths of 5$.\!\!'$96. North is at the top and east is to the left.
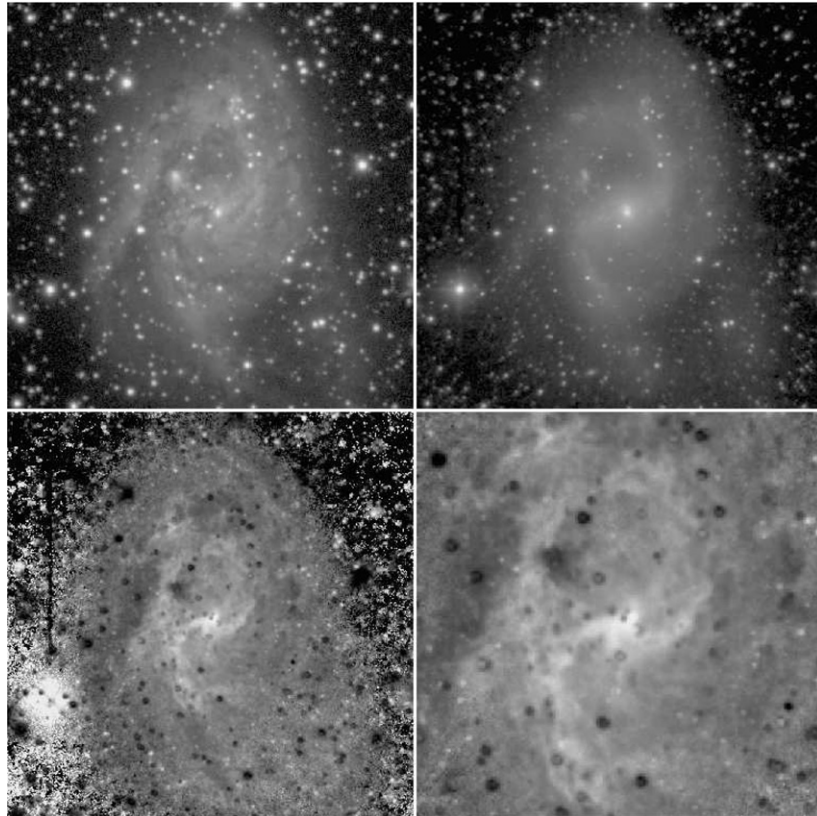
Figure 10. Images of NGC 6221. Upper left: *B*-band (Eskridge et al. 2002); upper right: K_s-band; lower left: $B - K_s$ color index map; lower right: same as at lower left, at twice the scale. The images are logarithmic in units of mag arcsec^{-2} and the main fields have side lengths of 3$.\!\!'$73. North is at the top and east is to the left. In the color index maps, central colors are uncertain owing to a seeing mismatch between the *B*- and K_s-band images.

Table 7
Maximum Relative Gravitational Torques and Spiral Contrasts

| Galaxy 1	Q_g 2	Q_b 3	Q_s 4	A_{2s} 5	A_{4s} 6	r_g 7	r_b 8	r_s 9	r_{2s} 10	r_{4s} 11
NGC 175	0.475	0.436	0.210	0.422	0.249	16.0	15.5	26.0	26.5	28.5
	±0.073	±0.064	±0.040	±0.050	±0.010					
NGC 521	0.176	0.175	0.067	0.218	0.149	13.0	13.5	54.0	57.5	66.5
	±0.025	±0.026	±0.013	±0.020	±0.020					
NGC 613	0.483	0.395	0.346	0.780	0.449	63.0	48.0	75.0	88.5	81.5
	±0.096	±0.064	±0.089	±0.078	±0.045					
NGC 986	0.586	0.436	0.497	1.220	0.733	46.5	35.0	63.0	62.5	63.5
	±0.106	±0.064	±0.132	±0.061	±0.037					
NGC 1300	0.573	0.502	0.232	0.789	0.346	60.5	59.0	123.5	117.5	118.5
	±0.090	±0.074	±0.063	±0.039	±0.017					
NGC 1566	0.234	0.153	0.230	0.611	0.316	75.0	27.0	74.5	68.0	66.5
	±0.041	±0.022	±0.046	±0.031	±0.016					
NGC 4593	0.343	0.341	0.064	0.332	0.200	45.5	45.5	60.0	98.5	75.5
	±0.055	±0.051	±0.024	±0.088	±0.059					
NGC 5101	0.233	0.227	0.043	0.216	0.066	40.0	40.0	100.0	84.5	59.5
	±0.033	±0.033	±0.026	±0.011	±0.017					
NGC 5335	0.425	0.422	0.049	0.107	0.136	20.0	20.0	46.5	47.5	47.5
	±0.061	±0.062	±0.010	±0.005	±0.007					
NGC 5365	0.102	0.106	0.013	0.063	0.018	38.0	37.0	43.0	67.5	65.5
	±0.015	±0.016	±0.005	±0.015	±0.018					
NGC 6221	0.421	0.400	0.261	0.455	0.197	28.0	28.0	48.0	49.5	66.5
	±0.076	±0.059	±0.080	±0.046	±0.020					
NGC 6384	0.112	0.127	0.106	0.255	0.106	18.5	19.0	50.0	53.5	79.5
	±0.019	±0.020	±0.019	±0.038	±0.016					
NGC 6782	0.183	0.180	0.037	0.283	0.112	23.0	23.0	57.0	42.5	38.5
	±0.026	±0.027	±0.009	±0.119	±0.068					
NGC 6907	0.384	0.272	0.349	0.714	0.371	27.0	24.0	44.5	37.5	32.5
	±0.084	±0.042	±0.085	±0.070	±0.029					
NGC 7155	0.185	0.185	0.031	0.333	0.089	22.0	22.0	61.0	67.5	54.5
	±0.027	±0.027	±0.009	±0.017	±0.004					
NGC 7329	0.322	0.313	0.153	0.486	0.109	27.0	27.0	55.5	84.5	72.5
	±0.049	±0.048	±0.035	±0.073	±0.011					
NGC 7513	0.660	0.666	0.114	0.132	0.214	27.0	27.0	43.5	63.5	75.5
	±0.117	±0.115	±0.023	±0.017	±0.011					
NGC 7552	0.409	0.401	0.100	0.406	0.309	41.5	41.0	62.0	85.5	73.5
	±0.065	±0.062	±0.037	±0.100	±0.100					
NGC 7582	0.427	0.417	0.110	0.291	0.157	57.0	56.0	69.0	108.0	83.5
	±0.069	±0.064	±0.036	±0.100	±0.050					
IC 1438	0.125	0.124	0.052	0.285	0.156	19.5	19.5	74.0	62.5	64.5
	±0.018	±0.018	±0.014	±0.014	±0.008					
IC 4290	0.532	0.522	0.079	0.635	0.309	20.0	20.0	50.0	51.5	56.5
	±0.077	±0.077	±0.018	±0.032	±0.015					
IC 5092	0.508	0.506	0.151	0.324	0.111	17.0	17.0	27.5	32.5	29.5
	±0.086	±0.075	±0.031	±0.039	±0.036					
UGC 10862	0.826	0.796	0.152	0.279	0.145	12.0	12.0	17.0	23.5	20.5
	±0.117	±0.117	±0.030	±0.098	±0.052					

Notes. Column 1: galaxy name; Column 2: total nonaxisymmetric maximum relative torque; Column 3: bar strength; Column 4: spiral strength; Column 5: spiral maximum $m = 2$ contrast; Column 6: spiral maximum $m = 4$ contrast; Columns 7–11: radii of Q_g, Q_b, Q_s, A_{2s}, and A_{4s} maxima in arcseconds.

the dominant feature in the relative Fourier amplitudes and is well fitted by a double Gaussian in all even terms to $m = 20$ at least. The spiral structure is weak in the K_s-band, and we obtain a bar class of 4 and a spiral class of 0.

NGC 5365. The K_s-band image in Figure 1 shows a well-defined early-type barred S0 with an extended disk and a trace of an outer ring. A clear secondary bar aligned nearly perpendicular to the primary bar is seen in this image, a feature already noted by Mulchaey et al. (1997; see also Erwin 2004). The two-dimensional decomposition gave a Sérsic index of $n = 1.8$ and a bulge-to-total luminosity ratio of 0.48, the latter a likely overestimate since the secondary bar was not fitted separately.

A double Gaussian was needed to represent the even Fourier terms in the primary bar of NGC 5365. Only the secondary bar provides any additional significant amplitude. In spite of the apparent strength of the bar, the significant bulge leads to a bar class of only 1.

NGC 6221. Both the bar and spiral arms in this galaxy show considerable dust content in the color index map in Figure 10. The outer spiral pattern is disturbed and the galaxy is likely interacting, possibly with neighbor NGC 6215 (Koribalski & Dickey 2004). The azimuthally averaged profile in Figure 18 smooths out much of this structure. The two-dimensional decomposition gave a Sérsic index of $n = 1.6$ and a B/T ratio of 9.1%. A symmetry-assumption mapping of
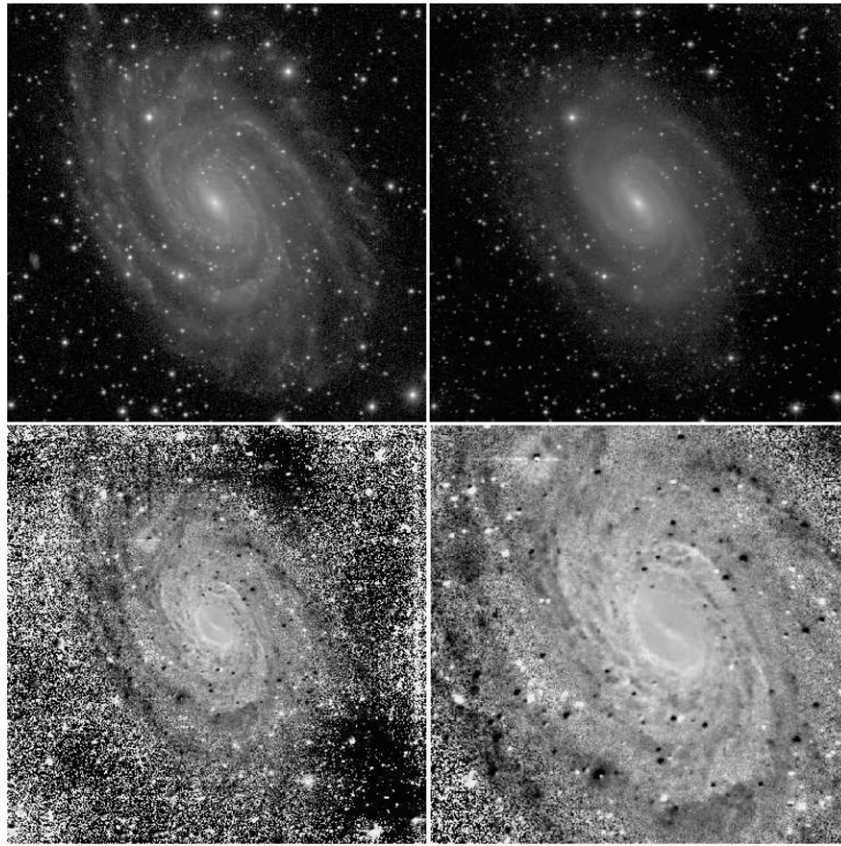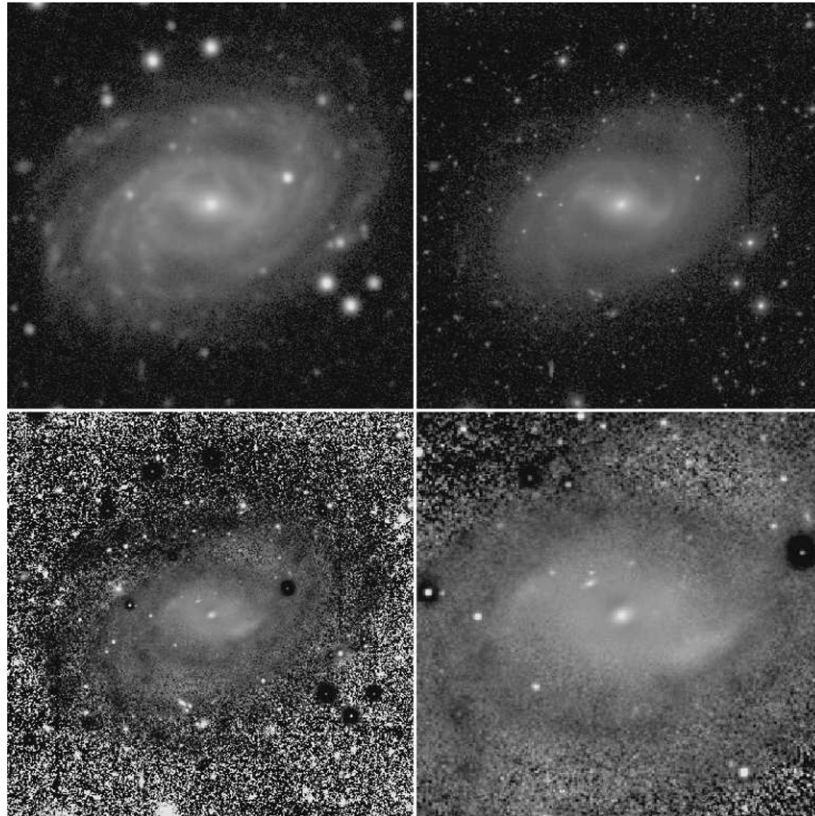
Figure 11. Images of NGC 6384. Upper left: B-band (S. C. Odewahn, deVA); upper right: K_s-band; lower left: $B - K_s$ color index map; lower right: same as at lower left, at twice the scale. The images are logarithmic in units of mag arcsec^{-2} and the main fields have side lengths of $6'.71$. North is at the top and east is to the left.
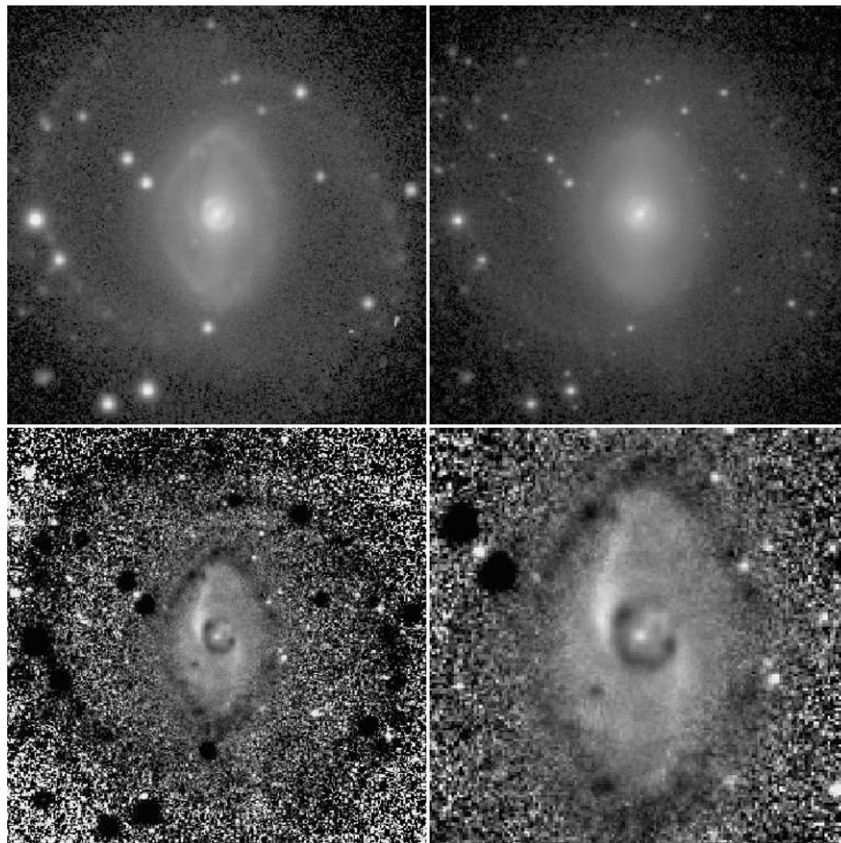
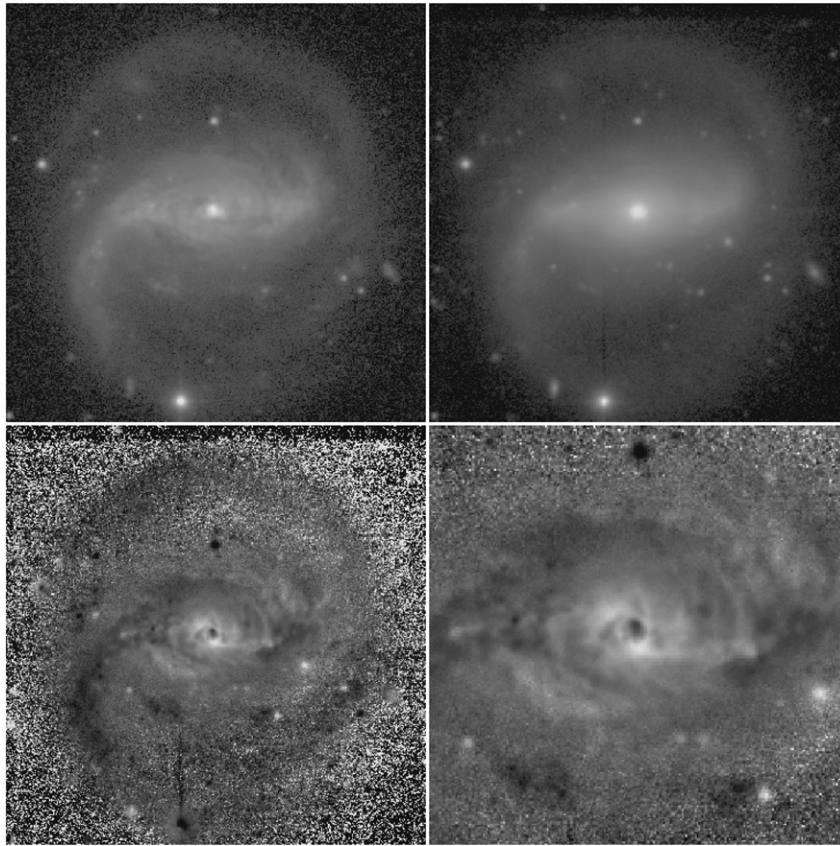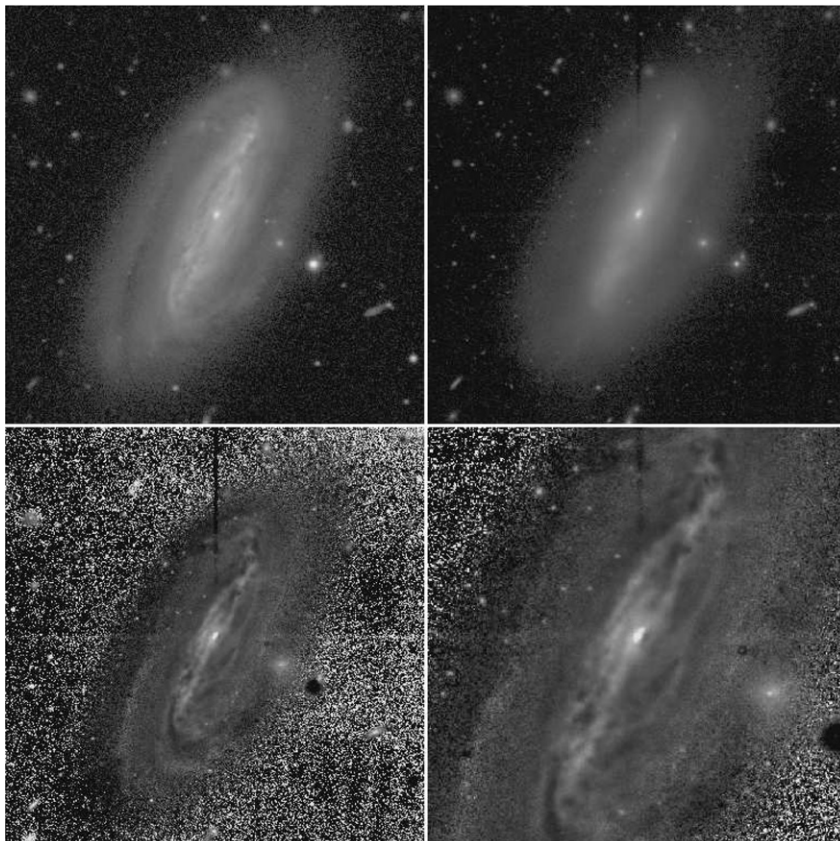**Figure 12.** Images of NGC 6782. Upper left: B-band (R. Buta, deVA); upper right: K_s-band; lower left: $B - K_s$ color index map; lower right: same as at lower left, at twice the scale. The images are logarithmic in units of mag arcsec^{-2} and the main fields have side lengths of $1'.49$. North is at the top and east is to the left.
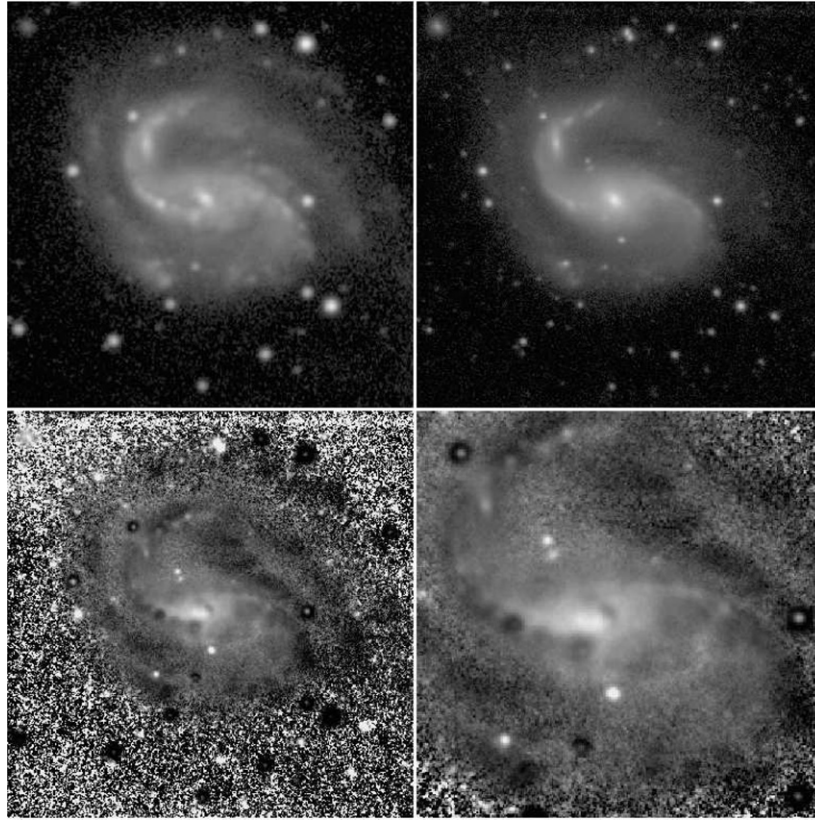
Figure 13. Images of NGC 6907. Upper left: B-band (B. Canzian, deVA); upper right: K_s-band; lower left: $B - K_s$ color index map; lower right: same as at lower left, at twice the scale. The images are logarithmic in units of mag arcsec^{-2} and the main fields have side lengths of $3'.62$. North is at the top and east is to the left. In the color index maps, central colors are uncertain owing to a seeing mismatch between the B and K_s-band images.

Figure 14. Images of NGC 7329. Upper left: B-band (G. B. Purcell, deVA); upper right: K_s-band; lower left: $B - K_s$ color index map; lower right: same as at lower left, at twice the scale. The images are logarithmic in units of mag arcsec^{-2} and the main fields have side lengths of $4'.41$. North is at the top and east is to the left. In the color index maps, central colors are uncertain owing to a seeing mismatch between the B and K_s-band images.

Figure 15. Images of NGC 7552. Upper left: *B*-band (Eskridge et al. 2002); upper right: K_s-band; lower left: $B - K_s$ color index map; lower right: same as at lower left, at twice the scale. The images are logarithmic in units of mag arcsec^{-2} and the main fields have side lengths of 3.73. North is at the top and east is to the left.

Figure 16. Images of NGC 7582. Upper left: *B*-band (Eskridge et al. 2002); upper right: K_s-band; lower left: $B - K_s$ color index map; lower right: same as at lower left, at twice the scale. The images are logarithmic in units of mag arcsec^{-2} and the main fields have side lengths of 5.30. North is at the top and east is to the left.
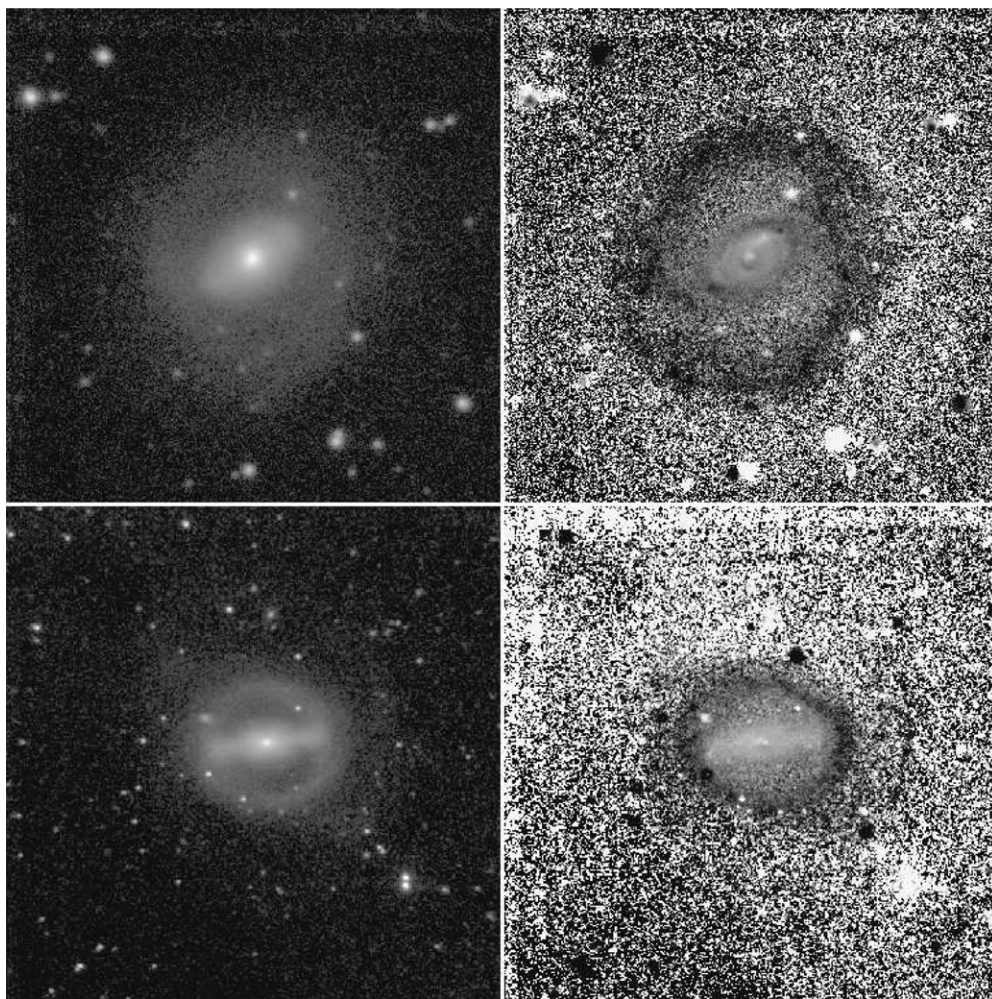
Figure 17. Images of IC 1438. Upper left: K_s-band; upper right: $B - K_s$; and IC 4290, lower left: K_s-band; lower right: $B - K_s$. Both B-band images are from the deVA (R. Buta). The images are logarithmic in units of mag arcsec^{-2} and the fields have side lengths of $3'.55$ for IC 1438 and $3'.76$ for IC 4290. North is at the top and east is to the left.

the relative Fourier intensity profiles of the bar was adopted in Figure 20. The spiral plus disk image in Figure 21 highlights some asymmetry in the bar not accounted for by this mapping.

NGC 6384. The multiarmed nature of the spiral pattern in the B-band is less evident in the K_s-band, where two arms seem to dominate (Figure 11). In the B-band image, a weak inner ring surrounds a relatively weak-looking bar. In the color index map, the inner ring surprisingly appears as a red feature. After visually mapping the feature, we find that the blue light inner ring has a projected diameter of 6.6 kpc, an axis ratio of 0.69, and a major axis position angle of $29°$, while the red $B - K_s$ inner ring has a diameter of 5.2 kpc, an axis ratio of 0.65, and a major axis position angle of $39°$. The dust ring is largely confined to the inner edge of the inner ring and is enhanced on the near side, east of the center. The B-band inner ring is not prominent in the color index map.

The two-dimensional decomposition gave a bulge with Sérsic index $n = 3.1$ and including 11.8% of the total K_s-band luminosity. The two-dimensional decomposition left some decomposition pinch in the deprojected image of NGC 6384. After removing this area, we find that the bar of NGC 6384 is largely a single Gaussian type.

NGC 6782. NGC 6782 is an exceptional ringed barred spiral. Although spiral structure is clearly evident in the B-band image

in Figure 12, the appearance of the galaxy in the K_s-band is as a late S0, or type (R)SB(r)0$^+$. The object is well known as a double-barred and triple-ringed system, and was recently interpreted as type (R_1R_2')SB(r)a by Buta et al. (2007). The $B - K_s$ color index map shows the strong leading dust lanes and nearly circular blue star-forming nuclear ring. The galaxy was the subject of a dynamical study by Lin et al. (2008), who interpreted the main features in terms of orbit resonances with the primary bar.

The two-dimensional decomposition shown in Figure 18 gave a Sérsic index $n = 2.1$ and a B/T of 40.8%. The latter is likely to be an overestimate because we have not taken into account the secondary bar. The bar of NGC 6782 is well represented by a double Gaussian, although this does not include all of the light of an extended oval that fills the deprojected minor axis of the outer ring. Bar–spiral separation gives a bar class of 2 and a spiral class of 0. The Q_b family of NGC 6782 is SAB.

NGC 6907. The deprojected K_s-band image in Figure 13 shows what could be interpreted as a bar in the inner regions, but the feature blends so smoothly with the spiral that the relative Fourier amplitudes do not clearly distinguish it and the phase of the $m = 2$ component is only approximately constant in the apparent bar region. The bar mapping in Figure 20 is imprecise since there is considerable asymmetry in the apparent bar, but nevertheless it provides a reasonable separation. The
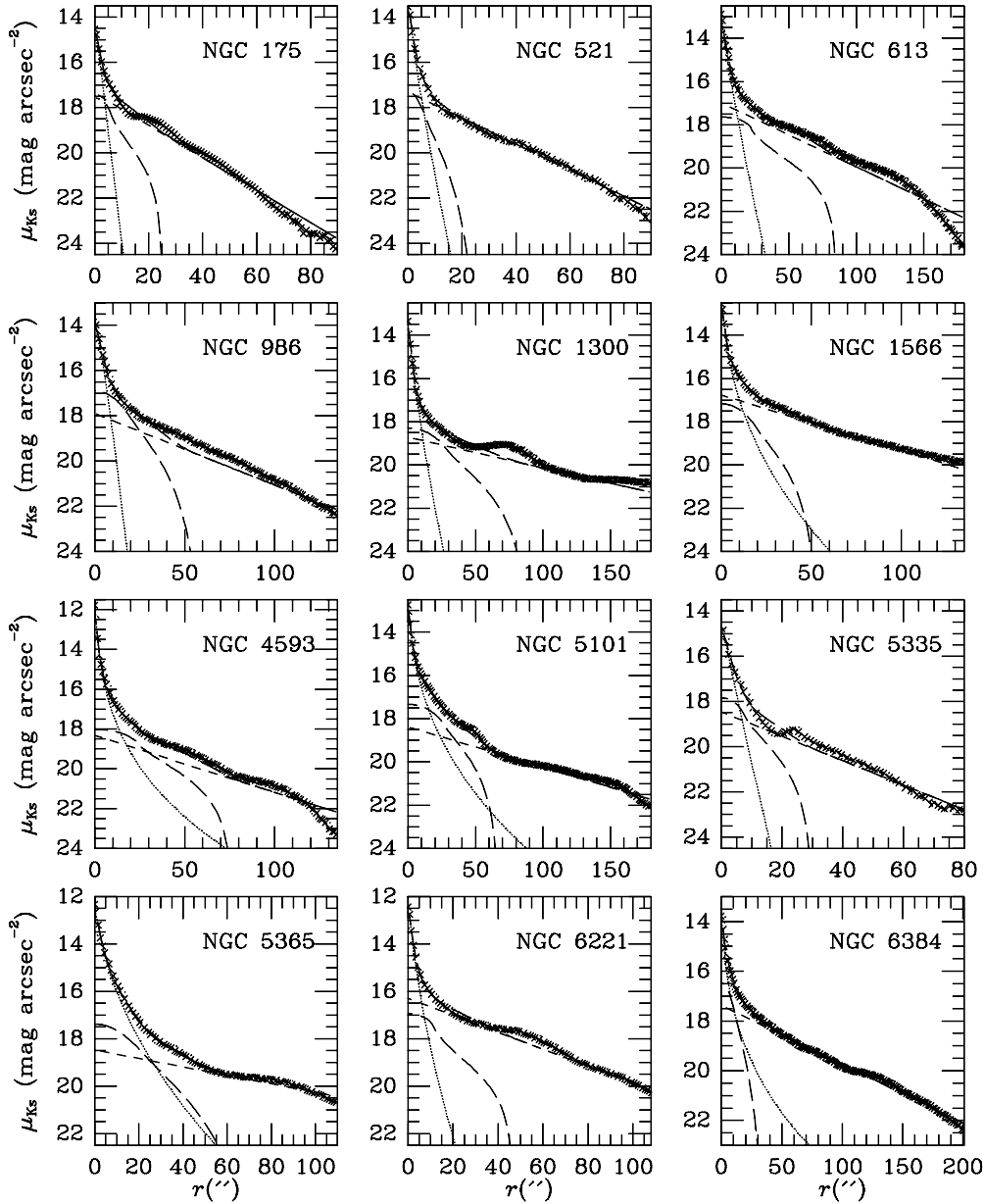
Figure 18. Azimuthally averaged K_s-band surface brightness profiles showing the results of the two-dimensional bulge/disk/bar decomposition fits. The luminosity distributions have been averaged within fixed ellipses having the orientation parameters listed in Table 1. Crosses refer to the observed profiles, dotted curves to the bulge models, short dashed lines to the disk model, long dashed curves to the bar model, and solid curves to the total model. These models assume a spherical bulge.

resulting bar and spiral classes are 3, with the spiral stronger than the bar.

The color index map in Figure 13 shows that red colors permeate the apparent bar region. The red arm, which breaks from the west end of the bar twists sharply eastward and is unusual.

The two-dimensional decomposition gave a nearly exponential bulge having a B/T of 12.7%.

NGC 7155. The K_s-band image in Figure 1 shows a well-defined SB0 galaxy with a prominent bar. The image also shows no evidence for a secondary bar. There is a faint trace of a diffuse inner ring.

The two-dimensional decomposition gave a Sérsic index of $n = 1.4$ and a B/T of 35.6%. Figure 20 shows that a single Gaussian well represents the relative Fourier amplitudes of the bar in NGC 7155. The bar class is 2 and there is no significant spiral.

NGC 7329. The images in Figure 14 show a well-developed intermediate type spiral where only the inner arms are prominent in the K_s-band. The color index map shows mostly red colors in the bar region, but the map is uncertain because the seeing on the *B*-band image is much poorer than on the K_s-band image. The two-dimensional decomposition gave a Sérsic index of $n = 1.4$ and a B/T of 21.1%. The deprojected K_s-band image shows some decomposition pinch in the inner parts of the bar. This is smoothed over in the bar plus disk image, but appears as a vertically oriented oval in the spiral plus disk image. We found that a single Gaussian well represents the relative Fourier profiles of the bar, although the $m = 2$ term is complicated by both the significant spiral structure and the decomposition pinch. The separated images gave a bar class of 3 and a spiral class of 1.

*NGC 7513.* The K_s-band image in Figure 2 shows a well-defined bar and faint spiral arms. The two-dimensional
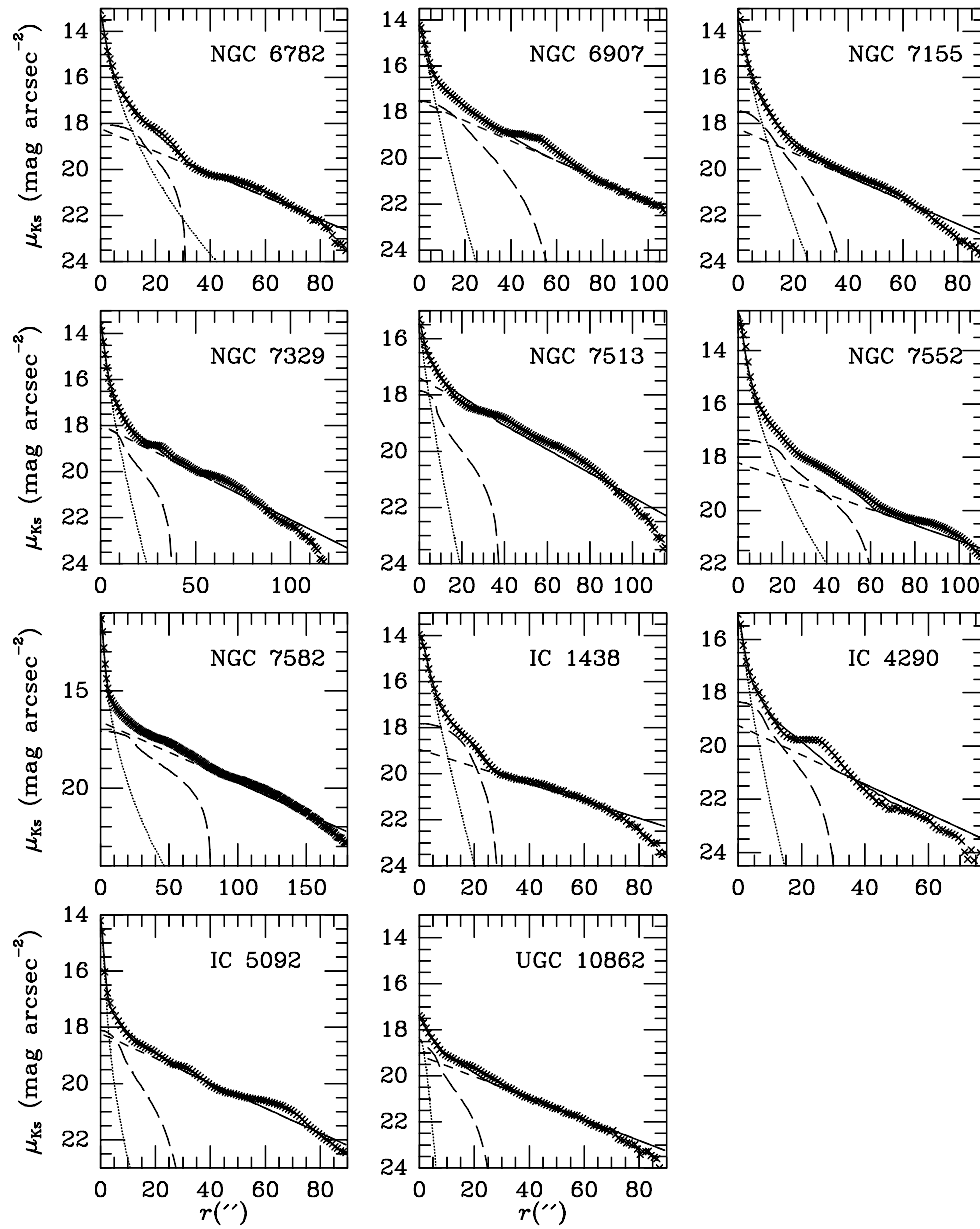
Figure 18. (Continued).

Table 8
Mean Parameters for Sample

Parameter	SG	DG
1	2	3
$\langle A_{2b} \rangle$	0.59 ± 0.07	0.82 ± 0.05
$\langle A_{4b} \rangle$	0.34 ± 0.05	0.46 ± 0.04
$\langle Q_g \rangle$	0.34 ± 0.09	0.34 ± 0.05
$\langle Q_b \rangle$	0.32 ± 0.08	0.32 ± 0.05
$\langle r_b/h_r \rangle$	1.17 ± 0.14	1.56 ± 0.17
$\langle B/T \rangle$	0.14 ± 0.05	0.26 ± 0.04
$\langle n \rangle$	1.71 ± 0.37	1.92 ± 0.24
No. of galaxies	7	11

Notes. Column 1: parameter; Column 2: mean values for single Gaussian bar Fourier profile galaxies; Column 3: mean values for double Gaussian bar Fourier profile galaxies.
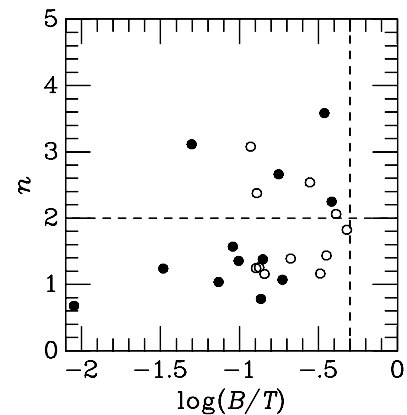
Figure 19. Graph of Sérsic index n and bulge-to-total luminosity ratio B/T for 23 barred galaxies. The filled circles are galaxies having $Q_b \geqslant 0.28$, and the open circles are galaxies having $Q_b < 0.28$. The dashed lines indicate limits for classical and pseudobulges from Kormendy & Kennicutt (2004). Points having $n < 2$ and $\log(B/T) < -0.3$ are considered pseudobulges.
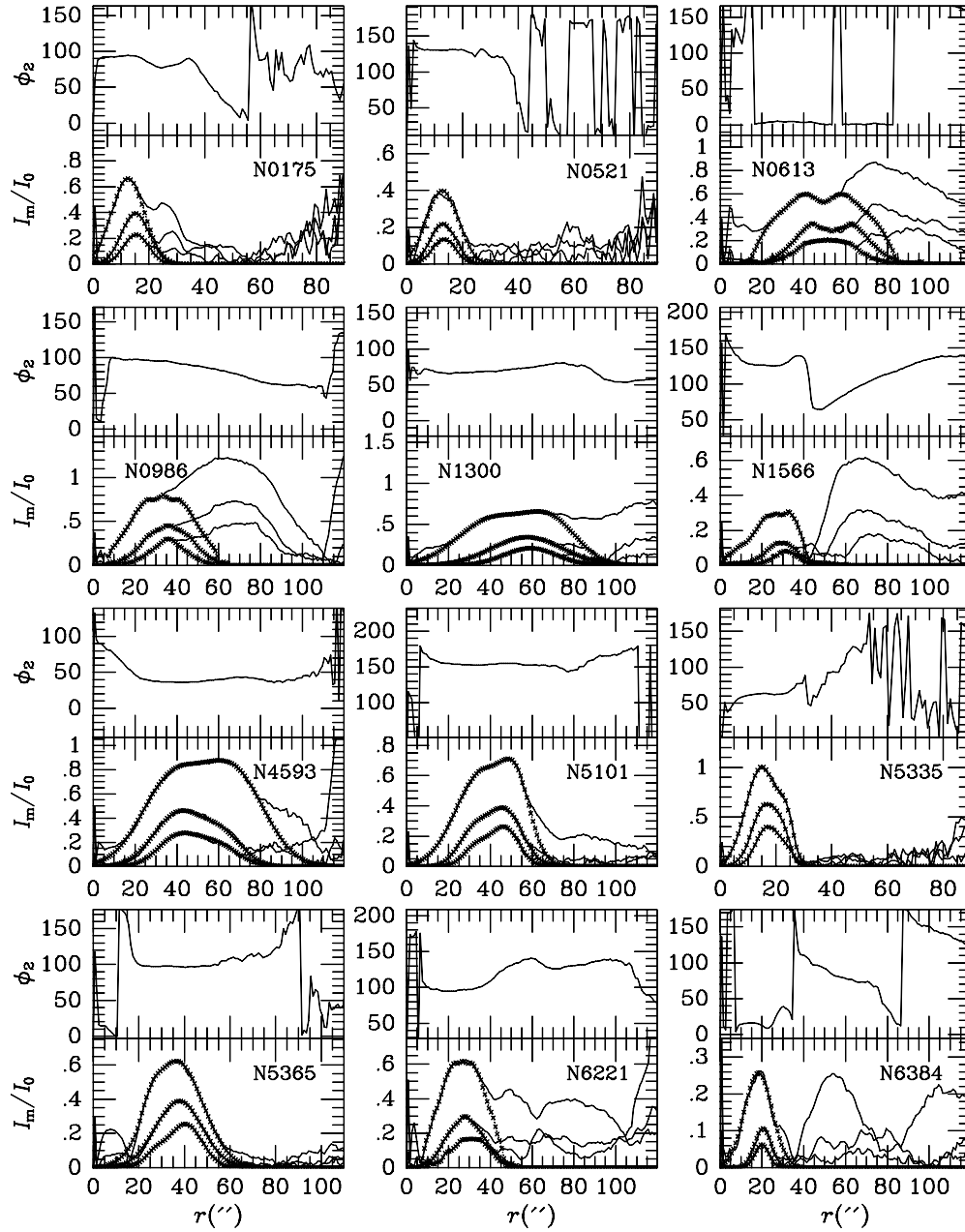
Figure 20. Plots of relative Fourier amplitudes I_m/I_0 ($m = 2, 4, 6$) and $m = 2$ phase ϕ_2 (degrees) for 23 galaxies. The crossings show mappings of the bar used for bar–spiral separation and estimation of bar and spiral strengths. Some of these mappings are based on the symmetry assumption, while others are based on single or double Gaussian fits.

decomposition (Figure 18) gave an approximately exponential bulge with a B/T of only 3.3%. The bar was found to be well represented by a double Gaussian for all even Fourier terms to $m = 20$ (Figure 20). However, we found that including only even Fourier terms provided a poor mapping of the bar. Our analysis in this case includes extrapolations of odd Fourier terms in the same manner as the even terms. Figure 21 shows that there is little residual asymmetry in the bar when we account for such terms. From the separated images, NGC 7513 is found to have a very strong bar with a bar class of 7 and a spiral class of 1. It has the weakest known spiral in the presence of one of the strongest known bars.

NGC 7552. The images in Figure 15 show a strong bar and conspicuous spiral pattern in a relatively face-on disk. The bar shows strong dust absorption, and there is a blue nucleus. The

two-dimensional decomposition gave a Sérsic index of $n = 2.2$ and a B/T of 38.4%. The relative Fourier amplitudes (Figure 20) show a dominant bar that is best represented by the symmetry assumption for $m = 2$ and a double Gaussian by all even terms having $m > 2$. The residual spiral plus disk image in Figure 21 shows some asymmetry in the bar region. From the separated images, the bar class is 4 while the spiral class is 1.

NGC 7582. Except for a higher inclination, this galaxy is very similar to NGC 7552. The bar is very dusty and the spiral is fairly conspicuous in the K_s-band (Figure 16). The two-dimensional decomposition gave a Sérsic index of $n = 2.7$ and a B/T of 17.8%. The relative Fourier amplitudes (Figure 20) are well fitted by double Gaussians in all even terms to $m = 20$. After deprojection, the images show strong decomposition pinch in the inner regions, and some asymmetry in the bar region is
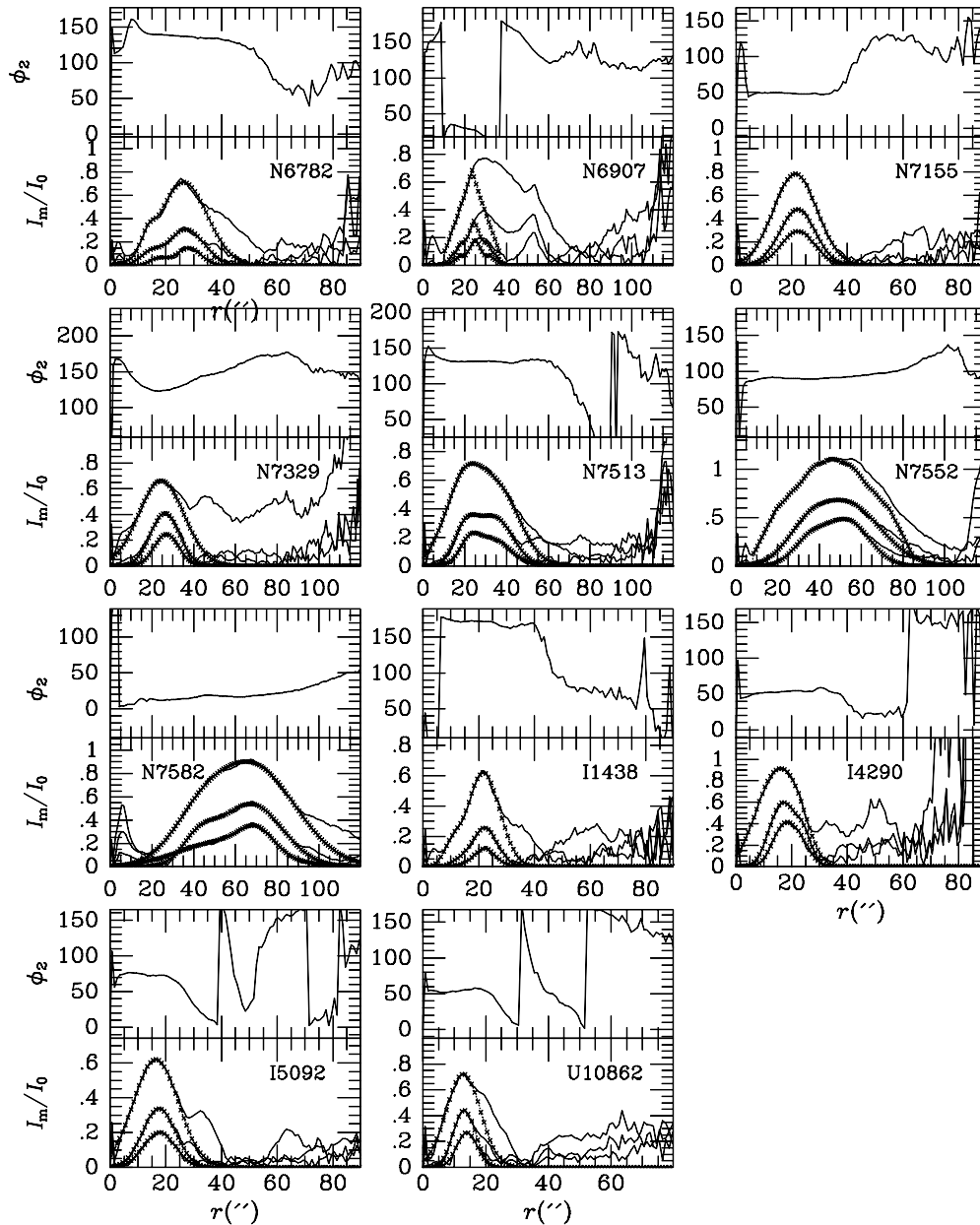
Figure 20. (Continued).

highlighted in the spiral plus disk image (Figure 21). The separated images gave a bar class of 4 and a spiral class of 1.

IC 1438. The K_s-band image in Figure 17 shows a nearly face-on, weakly barred galaxy with a faint outer ring. The color index map shows enhanced star formation in nuclear, inner, and outer rings/pseudorings. The two-dimensional decomposition (Figure 18) gave a nearly exponential bulge and a B/T of 32.5%. The mappings of the bar Fourier components in Figure 20 use a double Gaussian. The $m = 2$ term is more complicated than $m = 4$ and 6 because the primary bar is imbedded within a clear oval that contributes mainly to $m = 2$. From the separated images in Figure 21, the galaxy is bar class 1 and spiral class 1 with the bar stronger than the spiral.

IC 4290. The bar and inner ring are the most conspicuous features seen in the K_s-band image (Figure 17). Both features are also seen in the color index map. The galaxy is relatively face-on and a visual mapping of the deprojected inner ring gave

a diameter of 18.4 kpc, an axis ratio of 0.89, and (within 8°) an alignment nearly parallel to the bar. The bar itself has a strong inner boxy zone noted in previous studies by Buta & Crocker (1991) and Buta et al. (1998). The two-dimensional decomposition gave a nearly exponential bulge and a B/T of 14.1%. The relative Fourier amplitudes in the bar are well represented by double Gaussians for all even terms to $m = 18$ (Figure 20). The separated images (Figure 21) gave a bar class of 5 and a spiral class of 1.

IC 5092. The K_s-band morphology of this galaxy is in the unusual form of an s-shaped barred spiral encompassed by a conspicuous outer ring (Figure 2). The two-dimensional decomposition gave a Sérsic index of $n = 3.1$ and a B/T of 5.0% (Figure 18). A single Gaussian was adopted for the bar mapping in Figure 20. The separated images (Figure 21) gave a bar class of 5 and a spiral class of 2.

UGC 10862. The bar in this late-type spiral is unusual: it appears in the form of a highly elongated ring with ansae. This
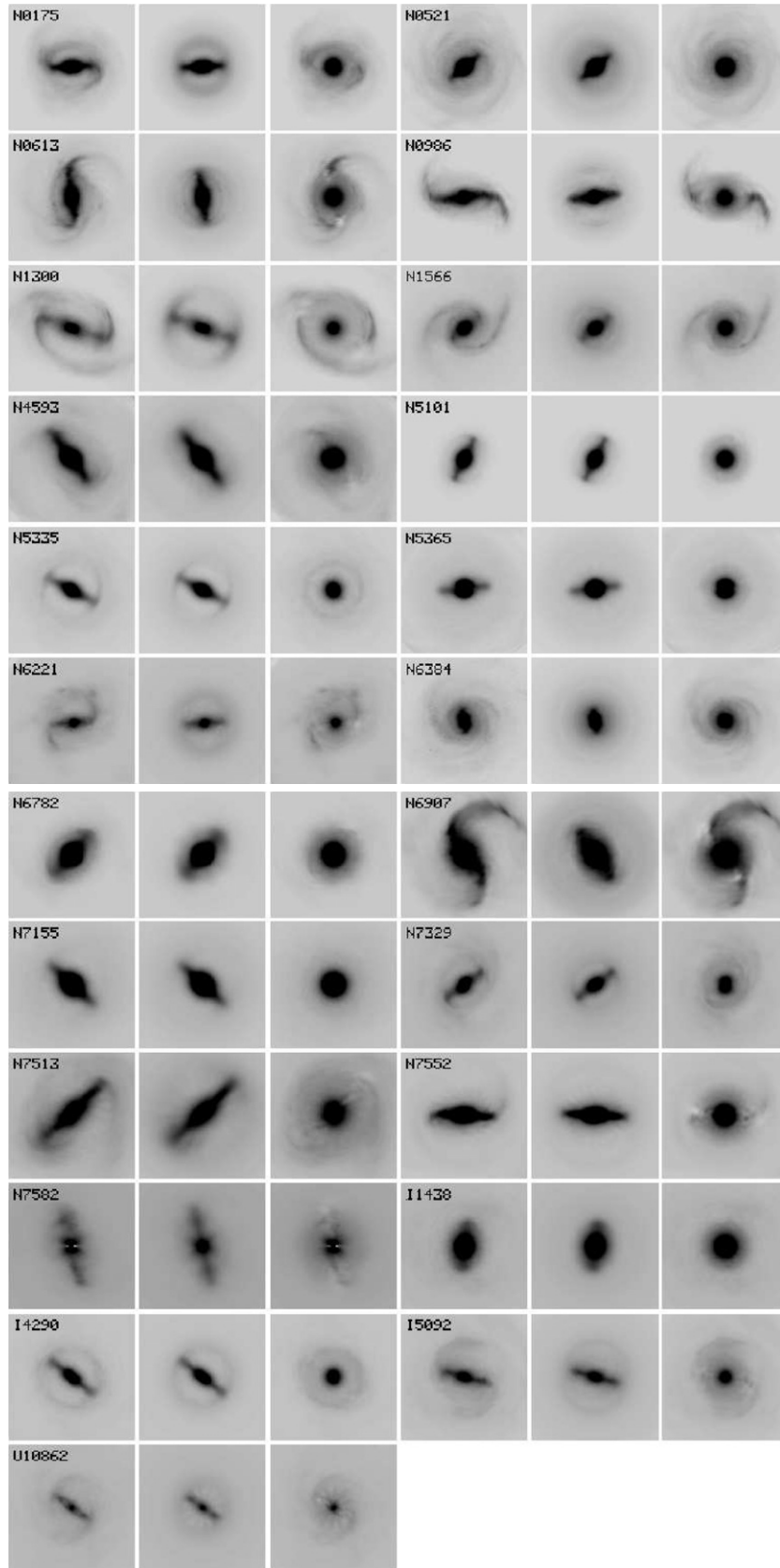
Figure 21. Bar–spiral separated images of the sample galaxies. Three images are shown for each galaxy (left to right): the deprojected K_s-band image cleaned of foreground and background objects (with the galaxy name at upper left), the bar plus disk image based on the mapping given in Figure 20, and the spiral plus disk image after bar removal. The images focus mainly on the inner regions and are in linear intensity units.
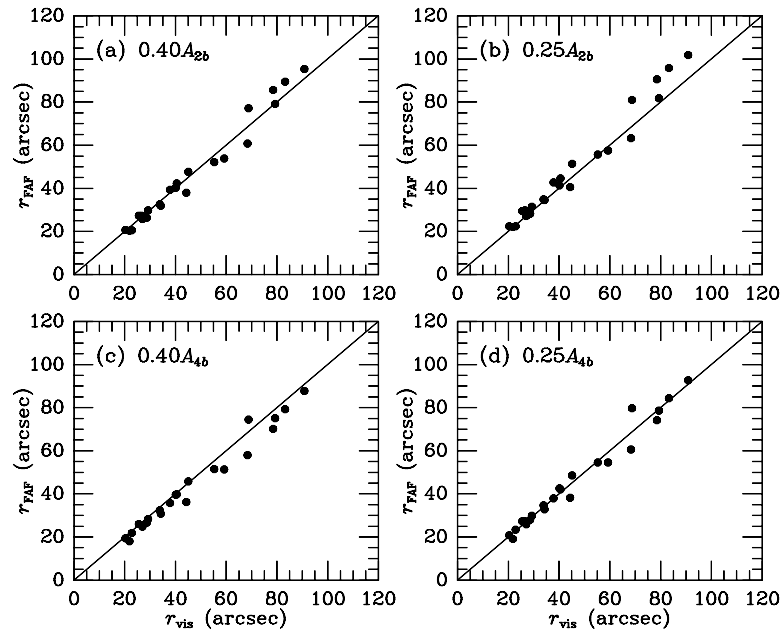
Figure 22. Graphs of Fourier-estimated bar radii vs. visual bar radii for 23 barred galaxies. The radii r_{FAF} are "Fourier amplitude fraction" radii for the indicated fractions of the bar contrast parameters A_{2b} and A_{4b}.
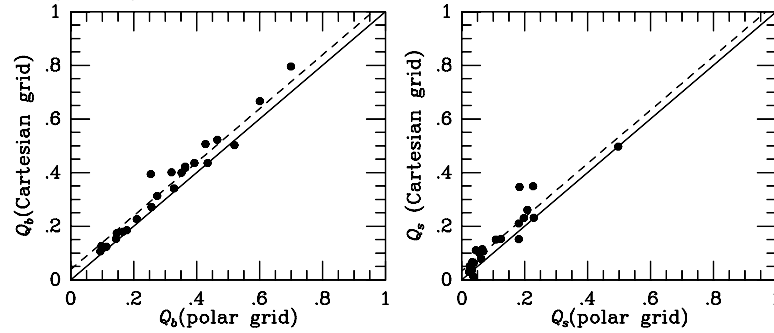
Figure 23. Comparison of bar and spiral strengths based on potentials derived from the Cartesian method (Quillen et al. 1994) and the polar grid method (Laurikainen & Salo 2002). The solid lines are for perfect correlation while the dashed lines allow for average offsets. The differences are not due to the integration method used but are most likely related to small differences in the treatment of the bulge and the vertical scale height, as well as the mappings of the maxima in different quadrants which are independent of the potential calculations.
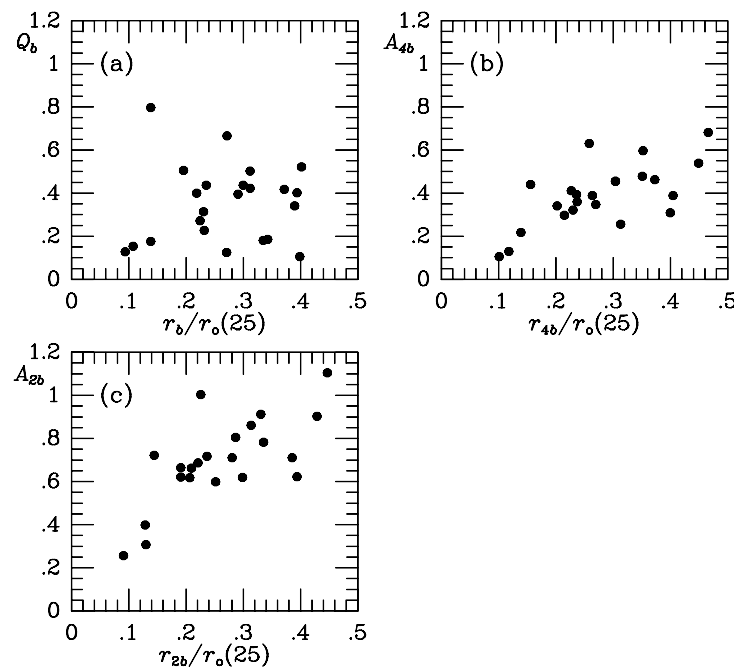
Figure 24. Graphs of bar strength and contrast with normalized radii for 23 barred galaxies.

character is shown best in the unsharp mask image in Figure 2. We have no optical images of this galaxy that can be used to determine the colors of the bar features. The two-dimensional decomposition gave a bulge with a Sérsic index of $n = 0.68$ and a B/T of 0.9%. The bulge is weak and the solution may not be reliable. The bar mapping in Figure 20 uses a single Gaussian representation and the separated images in Figure 21 gave a bar class of 8 and a spiral class of 2, the strongest bar in the sample.

9. DISCUSSION: DO THE STRONGER BARS HAVE STRONGER SPIRALS?

We investigate this issue not only using Q_s as a measure of spiral strength, but also the $m = 2$ and 4 spiral contrasts. The reason for including the spiral contrasts is because these can be considered the response to the spiral driver, the bar torque. The spiral torque Q_s is not the same as the response amplitude, but is diluted by the inner bulge and the bar radial force.

Figure 26 shows graphs of spiral contrast, spiral strength, and total maximum relative nonaxisymmetric torque strength versus bar strength Q_b, parameters all listed in Table 7. The Q_g versus Q_b plot is shown only to highlight that for a sample like ours, Q_g is also a good indicator of bar strength. The spiral contrasts A_{2s} and A_{4s} were estimated from the spiral plus disk images after separation of the bar. Note that the radii of these maxima (also listed in Table 7) are often comparable but can differ considerably.

Figure 26 shows that the spiral parameters A_{2s}, A_{4s}, and Q_s all have little correlation with Q_b. (We note that the strongest spiral occurs for intermediate values of Q_b.) We can nevertheless quantify the correlations with a few statistical tests using programs from Press et al. (1986). For the 23 galaxies, the linear correlation coefficient for the Q_s, Q_b plot is $r_\ell = 0.26$ and the null hypothesis of zero correlation is disproved only at the 22.5% significance level. The Spearman rank-order correlation coefficient is $r_{sp} = 0.41$ with a significance level of 5%, while the Kendall Tau rank coefficient is $\tau = 0.27$ with a significance level of 7%. Similar parameters for the A_{2s}, Q_b plot are $r_\ell = 0.16$ ($P_{r_\ell} < 47\%$), $r_{sp} = 0.24$ ($P_{r_{sp}} < 27\%$), and $\tau = 0.16$ ($P_\tau < 29\%$). Similar parameters for the A_{4s}, Q_b plot are $r_\ell = 0.27$ ($P_{r_\ell} < 22\%$), $r_{sp} = 0.39$ ($P_{r_{sp}} < 7\%$), and $\tau = 0.25$ ($P_\tau < 10\%$). For Q_s versus Q_b, the nonparametric rank-order coefficients do not completely rule out some correlation, but any correlation is weak. This is certainly partly due to the small number of galaxies in our present sample.

On the other hand, Q_s (and to some extent also A_{2s} and A_{4s}) will have an inverse correlation with Q_b due to the nature of bar–spiral separation. In a reliable separation, the radial profiles of the torques for the bar and spiral must lie wholly within the curve for the total torque. This leads to correlated uncertainties in Q_s and Q_b: if the bar is overestimated, then the spiral is underestimated and vice versa. In principle, this could weaken a real positive correlation between Q_s and Q_b if the radial torque curves for the bar and the spiral significantly overlap. However, for 19 of the 23 galaxies in our sample, the curves for the bar and the spiral (or other outer components) do not greatly overlap. The worst cases are NGC 613, 986, 1300, and 6907 (see Figure 21). Also, Buta et al. (2003) showed that a ±10% uncertainty in r_{2b} for the bar Fourier mapping would move a galaxy like NGC 6951 ($Q_b = 0.28$, $Q_s = 0.21$) along a line having $\Delta Q_s/\Delta Q_b = 0.044/0.021 = -2.1$. Thus, the correlated uncertainties may spread the points out more in Q_s than in Q_b. Since NGC 6951 is a very typical case of significant overlap between the bar and

the spiral (see Figure 2 of Buta et al. 2003), and the effect is still small, we conclude that correlated uncertainties between Q_s and Q_b are not causing a significant false correlation, nor masking completely a real one, between Q_s and Q_b over all the data points in our sample.

In Figure 27(c), we have combined our 23 galaxies with previous studies of bar and spiral strengths. This graph shows Q_s versus Q_b for 177 galaxies including the samples of Buta et al. (2005); Block et al. (2004), and six early-type spirals from Buta (2004), in addition to the AAT sample galaxies. For 15 galaxies having two sources of parameters, the values were averaged so that only a single point is plotted. The agreement between duplicate values, which involves calculations either from OSUBGS H-band images (the Q_{b1} and Q_{s1} values) or from K_s images (the Q_{b2} and Q_{s2} values), is shown in Figures 27(a), 27(b). No error bars are indicated on the individual points in Figure 27(c), but the errors would be similar to those shown in Figure 26(c). Figure 27(d) shows means of Q_s in bins of Q_b indicated by the dotted horizontal lines. The correlation analysis for this sample gives $r_\ell = 0.35$, $r_{sp} = 0.31$, and $\tau = 0.22$, all fairly low values but with probabilities indicating a significant correlation. We see in panel (b) that the means of Q_s do increase slightly with increasing Q_b. However, there is little correlation for $Q_b < 0.3$. The most interesting case added by the AAT sample is NGC 7513, which, as we have noted, is a class 7 bar, accompanied by only a weak class 1 spiral.

Figures 28 and 29 show plots of Q_s versus Q_b for the combined sample of 177 galaxies, but subdivided according to absolute blue magnitude and RC3 numerical stage (type) index. Several individual galaxies are labeled for reference. These plots reveal in a more convincing way that some correlation between Q_s and Q_b is indeed present. Among the more luminous galaxies, the strongest bars have the strongest spirals (NGC 1530, 7479). Among intermediate luminosity galaxies, NGC 1042 and 7412 stand out as spiral outliers at low Q_b, although they appear to be relatively normal late-types. NGC 1042 is classified as type SAB and NGC 7412 as type SB in RC3, yet only weak bars were detected in the near-infrared. These galaxies are also outliers in the rightmost panels in Figure 29. Only weak trends are evident in most of the panels, in the sense of a slow increase in spiral strength with increasing bar strength. Two of the strongest bars with the weakest spirals that we added, NGC 7513 and UGC 10862, are of lower luminosity than cases such as NGC 986, 1530, and 7479 that have very strong spirals. The most significant-looking correlations appear for later types.

On the basis of 17 spirals, Block et al. (2004) found a correlation between Q_s and Q_b and suggested that this implies that bars and spirals grow together and have the same pattern speed. Our comparably sized AAT sample also supports this finding but shows in addition that some very strong bars can have rather weak near-infrared spirals.

These results suggest that some spirals probably are driven responses to a strong bar, although we may need more information to decide which ones. We suggest that cases like NGC 986, 1530, and 7479 are in this category. All three of these objects have been analyzed using the potential-density phase-shift method (Zhang & Buta 2007), and all three show phase-shift distributions consistent with a single pattern speed of the main bar and spiral. Zhang & Buta (2007) discuss NGC 1530, while Buta & Zhang (2009a) provide the information on NGC 7479. The phase-shift results for NGC 986 are shown by Buta & Zhang (2009b), who also find that NGC 175 has a phase-shift distribution consistent with a decoupling between the spiral and the bar.
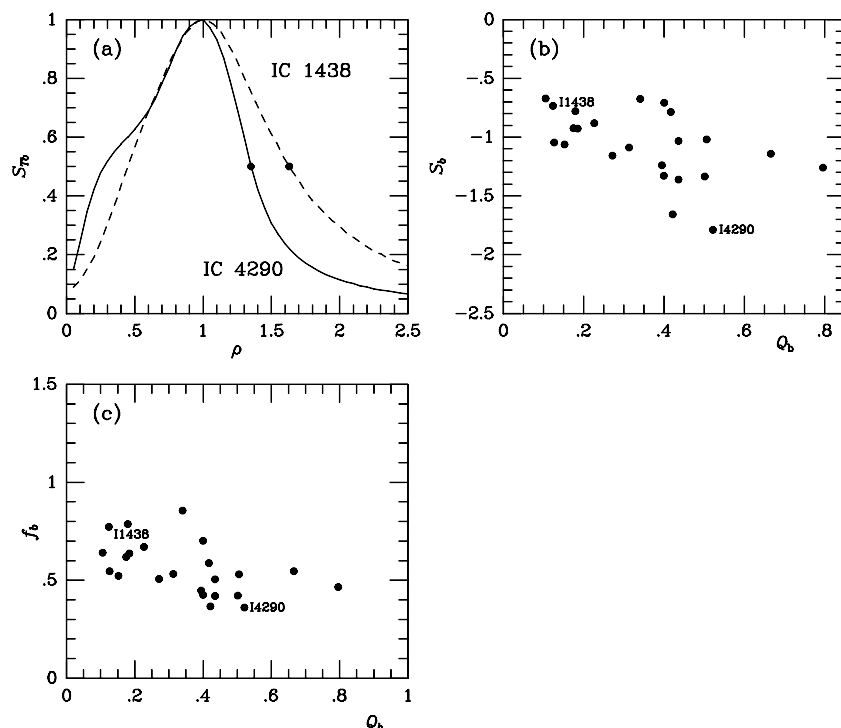
Figure 25. (a) Normalized bar torque profiles for the weakly barred galaxy IC 1438 and the strongly barred galaxy IC 4290. The parameters are $S_{\mathrm{Tb}} = Q_{\mathrm{Tb}}(r)/Q_b$ and $\rho = r/r_b$. (b) Plot of slope $dS_{\mathrm{Tb}}/d\rho$ at $S_{\mathrm{Tb}} = 0.5$ (filled circles in (a)). (c) A graph of the relative bar-end drop-off fraction defined as $f_b = \frac{(r(0.25Q_b)-r(0.75Q_b))}{r_b}$, vs. the bar strength Q_b. In (b) and (c), IC 1438 and IC 4290 are indicated.
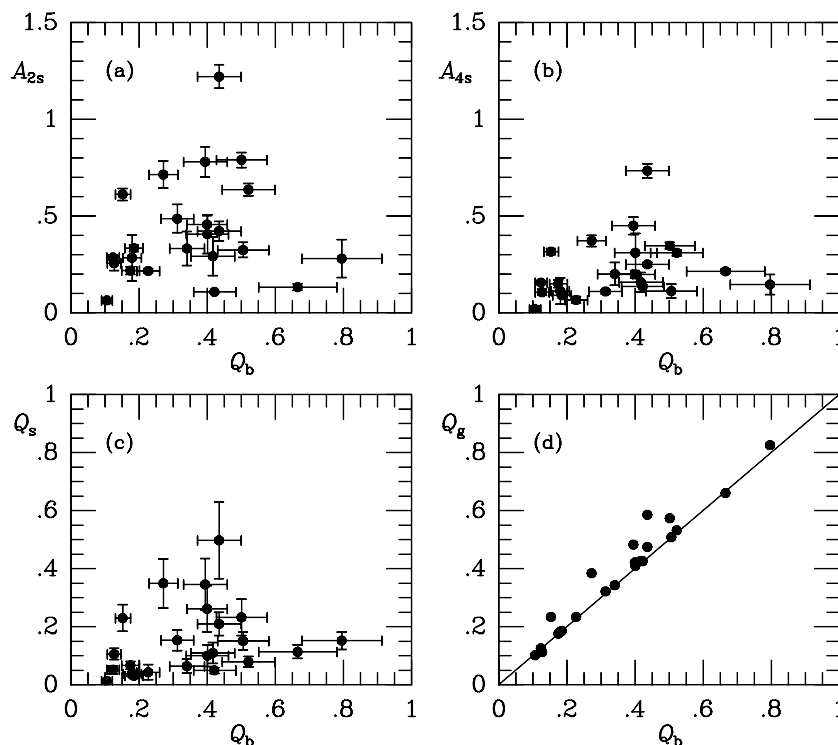

Figure 26. Graphs of (a) $m = 2$ spiral contrast A_{2s}, (b) $m = 4$ spiral contrast A_{4s}, (c) spiral strength Q_s, and (d) maximum total relative gravitational torque strength Q_g, vs. bar strength Q_b.

We suggested in Section 1 that bars may drive spirals only when the bar is growing or if there is gaseous dissipation. We suspect that there could be a saturated state where there is a bar but it cannot do much to drive a spiral. An example of such saturation is an SB0 galaxy. All the stars are in steady orbits,

and nothing is growing fast enough or dissipating fast enough to be a significant source of direction. A large galaxy with a small inner bar is also not likely to have a bar-driven spiral. A variety of factors undoubtedly conspire to make the scatter significant in a plot of Q_s versus Q_b.
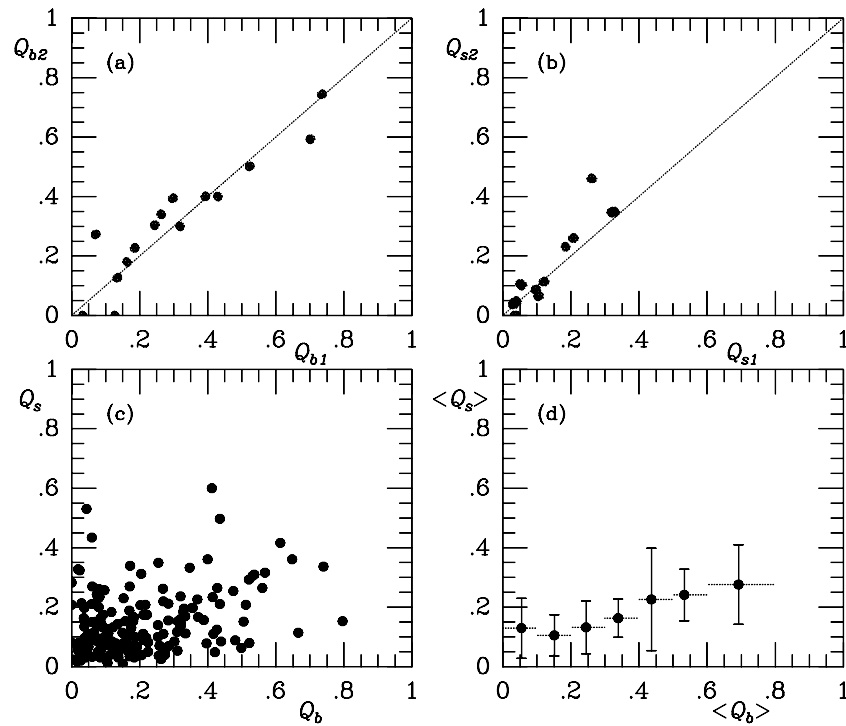
Figure 27. (a) Comparison between Q_b values from different studies. The Q_{b1} are values from Buta et al. (2005), while the Q_{b2} are values from this paper, Block et al. (2004), and Buta (2004). The solid line is for unit slope. (b) Comparison between Q_s values from different studies. The Q_{s1} are values from Buta et al. (2005), while the Q_{s2} are values from this paper, Block et al. (2004), and Buta (2004). The solid line is for unit slope. (c) Graph of spiral strength Q_s vs. bar strength Q_b for a combined sample of 177 galaxies including: the present AAT sample, the Block et al. (2004) sample, the Buta et al. (2005) sample, and a small sample of early-type spirals from Buta (2004). (c) Means and standard deviations of Q_s in bins of 0.1 in Q_b. The horizontal dashed lines indicate the Q_b bins within which Q_s is averaged. $\langle Q_b \rangle$ is the average of Q_b only within these bins and not at a given Q_s.
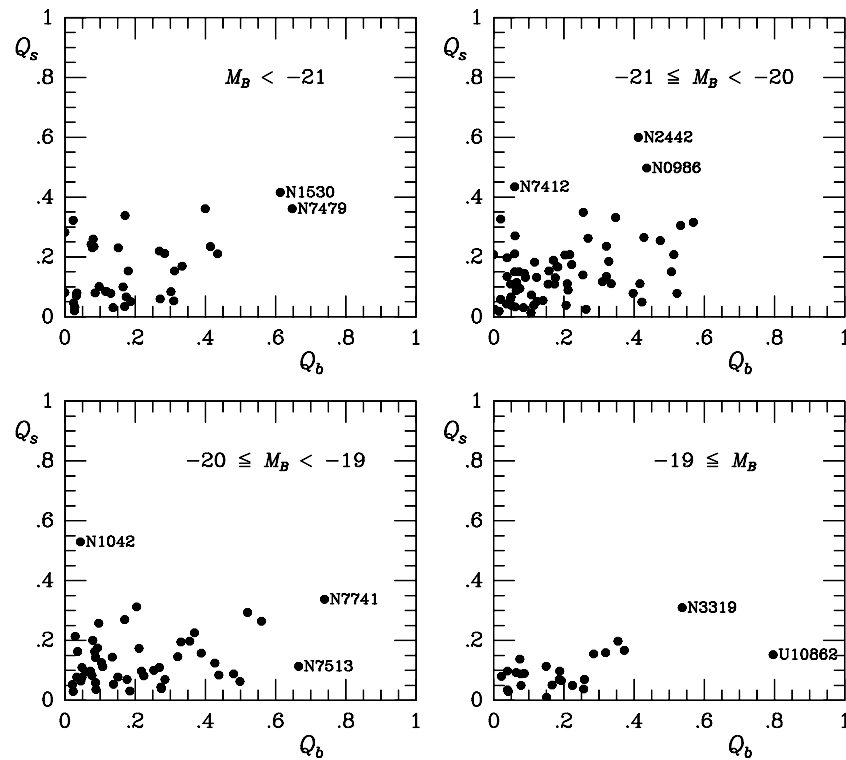
Figure 28. Graphs of spiral strength Q_s vs. bar strength Q_b for a combined sample of 177 galaxies subdivided according to absolute blue magnitude. Several outliers are labeled.
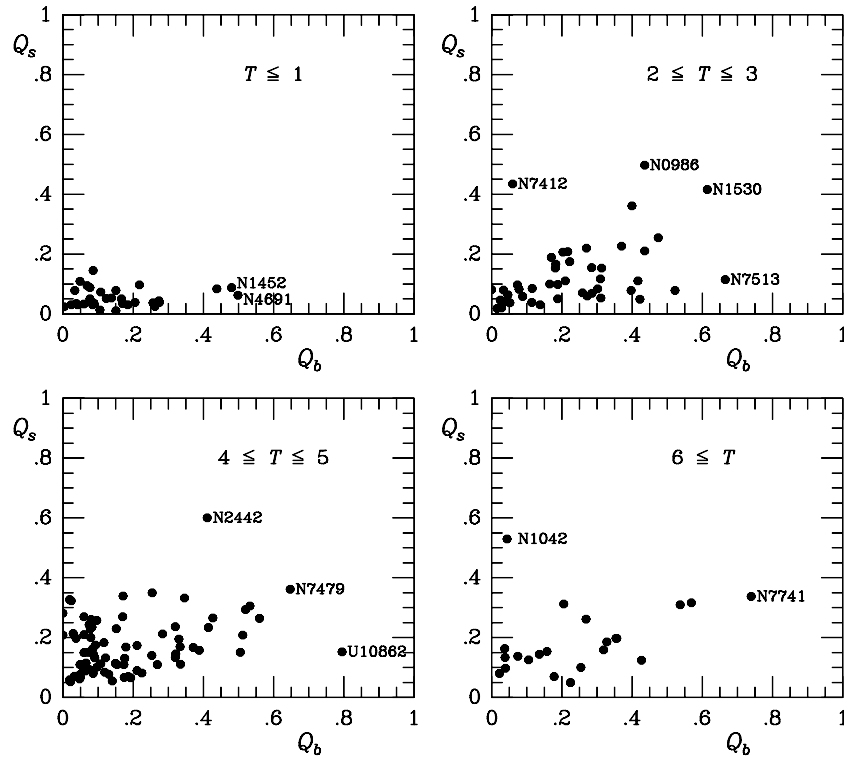
Figure 29. Graphs of spiral strength Q_s vs. bar strength Q_b for a combined sample of 177 galaxies subdivided according to RC3 stage index. Several outliers are labeled.

10. CONCLUSIONS

We have analyzed near-infrared images of 23 barred galaxies covering a wide range of types and apparent bar strengths. Using Fourier techniques, we have separated the bars from the spirals and have derived maximum relative bar and spiral torque strengths. Our results are as follows.

(1) The sample is morphologically diverse and includes strong two-armed barred spirals as well as multiarmed barred spirals.

(2) As in previous studies (e.g., Buta et al. 2005, 2006), the relative Fourier intensity amplitudes of some of the bars in this sample can be mapped with single and double Gaussian representations. Others can be mapped with the symmetry assumption (Buta et al. 2003).

(3) We showed that Fourier amplitude fractions from $m = 2$ and 4 bar Fourier profiles could be a useful way to define bar radii.

(4) We showed that stronger bars have relatively sharper ends. This could mean that the orbits crowd an outer resonance, as if the volume in phase space that contains bar-reinforcing orbits is nearly filled.

(5) In answer to our main question, we find weak but definite indications that stronger spirals are associated with stronger bars. This is consistent with our previous findings, but two of the galaxies in our present sample, NGC 7513 and UGC 10862, show that exceptionally strong bars can have weak near-infrared spirals. Some galaxies with strong bars, like NGC 986, do have strong spirals. Because spirals having bars with $Q_b > 0.4$ are very rare, our study is still affected by small number statistics at the strong bar end.

Thus, our main conclusion of this study is similar to that of Block et al. (2004): some bars and spirals probably grow together in a global disk instability, leading to the average increase of Q_s with Q_b for $Q_b > 0.3$. For $Q_b < 0.3$, bars and spirals may be more independent features in general. Cases where the strength of the bar and the spiral are comparably large, as in NGC 986, could be genuine "bar-driven" spirals. Nevertheless, the existence of cases like NGC 7513 and UGC 10862, which lie in what was previously an empty region in the Q_s, Q_b plot, shows that other factors probably complicate the relationship between bar and spiral torque strengths.

Although our analysis did not provide a definitive answer to the question posed in the title of this paper, owing in part to the limitations of our samples as well as the depth and quality of some of the near-IR images used, this situation will change soon with the *Spitzer Survey of Stellar Structure in Galaxies* (S^{4}G; Sheth et al. 2009). This survey will provide a nearly complete sample of 2300 galaxies of all types within 40 Mpc to a depth that would be very difficult to achieve in the K_s-band from the ground. With such a large sample, we can improve the statistics in all regions of the Q_s, Q_b diagram and further examine the questions we have raised here.

This research has made use of the NASA/IPAC Extragalactic Database (NED), which is operated by the Jet Propulsion Laboratory, California Institute of Technology, under contract with NASA.

REFERENCES

Athanassoula, E., & Misiriotis, A. 2002, MNRAS, 330, 35

Block, D. L., Buta, R., Knapen, J. H., Elmegreen, D. M., Elmegreen, B. G., & Puerari, I. 2004, AJ, 128, 183

Block, D. L., Puerari, I., Frogel, J. A., Eskridge, P. B., Stockton, A., & Fuchs, B. 1999, Ap&SS, 269, 5

Block, D. L., & Wainscoat, R. J. 1991, Nature, 353, 48

Böker, T., Falcón-Barroso, J., Schinnerer, E., Knapen, J. H., & Ryder, S. 2008, AJ, 135, 479

Buta, R. 1995, ApJS, 96, 39

Buta, R. 2004, Astrophys. Space Sci. Library, 319, 101

Buta, R., & Block, D. L. 2001, ApJ, 550, 243

Buta, R., Block, D. L., & Knapen, J. H. 2003, AJ, 126, 1148

Buta, R. J., Corwin, H. G., & Odewahn, S. C. 2007, The de Vaucouleurs Atlas of Galaxies (Cambridge: Cambridge Univ. Press) (deVA)

Buta, R., & Crocker, D. A. 1991, AJ, 102, 1715

Buta, R., Laurikainen, E., & Salo, H. 2004, AJ, 127, 279

Buta, R., Laurikainen, E., Salo, H., Block, D. L., & Knapen, J. H. 2006, AJ, 132, 1859

Buta, R., Vasylyev, S., Salo, H., & Laurikainen, E. 2005, AJ, 130, 506

Buta, R., & Zhang, X. 2009a, arXiv:0903.4695

Buta, R., & Zhang, X. 2009b, arXiv:0903.2008

Buta, R., et al. 1998, AJ, 116, 1142

Combes, F., & Sanders, R. H. 1981, A&A, 96, 164

de Grijs, R. 1998, MNRAS, 299, 595

de Vaucouleurs, G., & Buta, R. 1980, ApJS, 44, 451

de Vaucouleurs, G., de Vaucouleurs, A., Corwin, H. G., Buta, R. J., Paturel, G., & Fouque, P. 1991, Third Reference Catalog of Bright Galaxies (New York: Springer) (RC3)

Elmegreen, D. M., & Elmegreen, B. G. 1982, MNRAS, 201, 1021

Elmegreen, B. G., & Elmegreen, D. M. 1985, ApJ, 288, 438

Elmegreen, B. G., Elmegreen, D. M., & Hirst, A. C. 2004, ApJ, 612, 191

Elmegreen, B. G., Elmegreen, D. M., Knapen, J. H., Buta, R. J., Block, D. L., & Puerari, I. 2007, ApJ, 670, L97

Erwin, P. 2004, A&A, 415, 941

Erwin, P. 2005, MNRAS, 364, 283

Eskridge, P. B., et al. 2002, ApJS, 143, 73

Gadotti, D., Athanassoula, E., Carrasco, L., Bosma, A., de Souza, R. E., & Recillas, E. 2007, MNRAS, 381, 943

Galaz, G., Villalobos, A., Infante, L., & Donzelli, C. 2006, AJ, 131, 2035

Hackwell, J. A., & Schweizer, F. 1983, ApJ, 265, 643

Hameed, S., & Devereaux, N. 1999, AJ, 118, 730

Jogee, S., et al. 2004, ApJ, 615, 105

Kennicutt, R. C., et al. 2003, PASP, 115, 928

Knapen, J. H., Shlosman, I., & Peletier, R. F. 2000, ApJ, 529, 93

Kohno, K., et al. 2008, PASJ, 60, 457

Koribalski, B., & Dickey, J. M. 2004, MNRAS, 348, 1255

Kormendy, J., & Kennicutt, R. 2004, ARA&A, 42, 603

Kormendy, J., & Norman, C. A. 1979, ApJ, 233, 539

Laurikainen, E., & Salo, H. 2002, MNRAS, 337, 1118

Laurikainen, E., Salo, H., & Buta, R. 2004, ApJ, 607, 103

Laurikainen, E., Salo, H., & Buta, R. 2005, MNRAS, 362, 1319

Laurikainen, E., Salo, H., Buta, R., & Knapen, J. H. 2007, MNRAS, 381, 401

Laurikainen, E., Salo, H., Buta, R., Knapen, J., Speltincx, T., & Block, D. L. 2006, MNRAS, 132, 2634

Lin, L.-H., Yuan, C., & Buta, R. 2008, ApJ, 684, 1048

Lynden-Bell, D., & Ostriker, J. P. 1967, MNRAS, 136, 293

Marinova, I., & Jogee, S. 2007, ApJ, 659, 1176

Menendez-Delmestre, K., Sheth, K., Schinnerer, E., Jarrett, T., & Scoville, N. 2007, ApJ, 657, 790

Mulchaey, J. S., Regan, M. W., & Kundu, A. 1997, ApJS, 110, 299

Peeples, M. S., & Martini, P. 2006, ApJ, 652, 1097

Press, W. H., et al. 1986, Numerical Recipes (Cambridge: Cambridge Univ. Press)

Quillen, A. C., Frogel, J. A., & González, R. A. 1994, ApJ, 437, 162

Regan, M., & Elmegreen, D. 1997, AJ, 114, 965

Sandage, A. 1961, The Hubble Atlas of Galaxies, Carnegie Inst. of Washington Publ. No. 618

Sérsic, J. L. 1968, Atlas de galaxias Australes (Cordoba, Argentina: Observatorio Astronomico)

Sheth, K., et al. 2008, ApJ, 675, 1141

Sheth, K., et al. 2009, Spitzer Proposal ID No. 60007

Toomre, A. 1969, ApJ, 158, 899

Toomre, A. 1981, in The Structure and Evolution of Normal Galaxies, ed. S. M. Fall (Cambridge: Cambridge Univ. press), 111

Verley, S., Combes, F., Verdes-Montenegro, L., Bergond, G., & Leon, S. 2007, A&A, 474, 43

Yuan, C., & Kuo, C.-L. 1997, ApJ, 486, 750

Zhang, X., & Buta, R. 2007, AJ, 133, 2584